A simple direct-forcing immersed boundary projection method with prediction-correction for fluid-solid interaction problems

Tzyy-Leng Horng[a], Po-Wen Hsieh[b], Suh-Yuh Yang[c,d,*], Cheng-Shu You[c]

[a] *Department of Applied Mathematics, Feng Chia University, Xitun District, Taichung City 40724, Taiwan*
[b] *Department of Applied Mathematics, National Chung Hsing University, South District, Taichung City 40227, Taiwan*
[c] *Department of Mathematics, National Central University, Jhongli District, Taoyuan City 32001, Taiwan*
[d] *National Center for Theoretical Sciences, National Taiwan University, Da'an District, Taipei City 10617, Taiwan*

A B S T R A C T

In this paper, we propose a simple and novel direct-forcing immersed boundary (IB) projection method in conjunction with a prediction-correction (PC) process for simulating the dynamics of fluid-solid interaction problems, in which each immersed solid object can be stationary or moving in the fluid with a prescribed velocity. The method is mainly based on the introduction of a virtual force which is distributed only on the immersed solid bodies and appended to the fluid momentum equations to accommodate the internal boundary conditions at the immersed solid boundaries. More specifically, we first predict the virtual force on the immersed solid domain by using the difference between the prescribed solid velocity and the computed velocity, which is obtained by applying the Choi–Moin projection scheme to the incompressible Navier–Stokes equations on the entire domain including the portion occupied by the solid bodies. The predicted virtual force is then added to the fluid momentum equations as an additional forcing term and we employ the same projection scheme again to correct the velocity field, pressure and virtual force. Although this method is a two-stage approach, the computational cost of the correction stage is rather cheap, since the associated discrete linear systems need to be solved in the correction stage are same with that in the prediction stage, except the right-hand side data terms. Such a PC procedure can be iterated to form a more general method, if necessary. The current two-stage direct-forcing IB projection method has the advantage over traditional one-stage direct-forcing IB projection methods, consisting of the prediction step only, by allowing much larger time step, since traditional methods generally request quite small time step for flow field relaxed and adjusted to the solid body movement even using implicit scheme. Numerical experiments of several benchmark problems are performed to illustrate the simplicity and efficient performance of the newly proposed method. Convergence tests show that the accuracy of the velocity field is super-linear in space in all the 1-norm, 2-norm, and maximum norm. We also find that our numerical results are in very good agreement with the previous works in the literature and one correction at each time step appears to be good enough for the proposed PC procedure.

1. Introduction

In this paper, we will propose a simple and novel direct-forcing immersed boundary (IB) projection method with prediction-correction (PC) for simulating the dynamics of incompressible viscous flows interacting with rigid solid bodies, where each immersed solid object can be stationary or moving in the fluid with a prescribed velocity. As is well known, the study of fluid-structure interaction (FSI) is of great importance in many applications of sciences and engineering, and it usually involves complex structure geometries. The body-fitted approach is a conventional method that is frequently used to simulate flow with a complex boundary. In that approach, the incompressible Navier–Stokes equations are spatially discretized on a curvilinear or unstructured grid that conforms to the immersed structure boundaries. Therefore, the boundary conditions such as the no-slip condition can be imposed easily. However, the body-fitted discretizations have to re-mesh the spatial domain at every time step correspondingly when the body deforms or moves in the fluid. Since the grid generation can become a large computational overhead, it would be desirable to avoid the need of re-meshing at each time step. Even the arbi-

* Corresponding author at: Department of Mathematics, National Central University, Jhongli District, Taoyuan City 32001, Taiwan.
E-mail addresses: tlhorng123@gmail.com (T.-L. Horng), pwhsieh@nchu.edu.tw (P.-W. Hsieh), syyang@math.ncu.edu.tw (S.-Y. Yang).

trary Lagrangian–Eulerian method still needs remedying for every several time steps to avoid the deterioration of grid quality. Thus, one should seek the help of the Cartesian grid based non-boundary conforming methods, such as the so-called IB method, to address the complex FSI problems.

It is well known that the IB method was originally introduced by Peskin in the 1970s to model blood flow in the heart and through heart valves (cf. [49,50]). In recent years, it has evolved into a simple but powerful method for formulating the interaction between viscous incompressible fluid and one or more structures immersed in it; see e.g., [10,24,32–34,36–38,41,42,47,51,53–55,60–62,67] and many references cited therein. In the traditional IB method, an Eulerian description is used to describe the fluid dynamics, while the Lagrangian representation is used to describe the surface of immersed object. Each immersed boundary exerts a singular force on the fluid and at the same time moves with the local fluid velocity when the velocity of the immersed object is not prescribed. The interaction between immersed boundary and fluid can be represented by a contribution to a force density term in the fluid momentum equations by means of the Dirac delta function. This results in a single set of governing equations of motion to hold in the entire domain without any internal boundary conditions. Instead of generating a boundary-fitted grid for regions exterior and interior to the immersed boundary at each time step, the spatial discretization of the IB method is implemented over Cartesian grids for the entire domain, and the immersed boundary is discretized by a set of Lagrangian marker points that are not constrained to lie on the grids. In the meantime, the Eulerian and Lagrangian variables are linked by the interaction equations that involve a smoothed approximation to the Dirac delta function.

According to the way that the singular force would be generated, the IB method can be generally categorized as either the feedback-forcing approach or the direct-forcing approach [45]. In the feedback-forcing approach, the singular forcing term is determined by using the differences between the expected displacement and velocity and the computed ones on the immersed boundary with two negative penalty parameters. These two negative parameters are obtained semi-empirically and usually impose restrictive stability conditions on the size of time step. Although this approach has proved to be rather capable of handling FSI problems of flows past stationary or moving cylinder, it sometimes have severe stability problems by the inherent feedback nature of the method. The feedback-forcing IB approach has been studied in recent years by many researchers, such as Goldstein et al. [19], Hsieh et al. [24], Lai and Peskin [36], Saiki and Biringen [52], Silva et al. [41], just to name a few. On the other hand, to tackle the difficulties arising in the feedback-forcing approach, the direct-forcing IB approach was introduced by Yu [67] and Fadlun et al. [17]. In this approach, the external force term is directly deduced from the momentum equations by setting the velocity at boundary points of the immersed object to the desired velocity using interpolation/distribution functions. In this manner, the boundary conditions can be approximately satisfied when combined with a projection scheme in practical computations. Compared with the feedback forcing, the direct forcing is rather straight forward, because there are no unknown parameters that should be determined in the formulation. The basic idea of the direct-forcing approach has been used and developed successfully in several further applications, see e.g., [2,15,22,26,29,40,44,59,61,64,67,68], etc.

In the work of Noor et al. [48], they proposed a new direct-forcing IB method combined with the projection scheme for simulating the dynamics of fluid-solid interaction problems, in which a virtual force for the solid body is added to the incompressible Navier–Stokes equations to accommodate the interaction between the fluid and solid. The most characteristic feature of such approach is that the virtual force is not just distributed on immersed solid boundary, but is actually distributed on the whole solid body. In the projection computations, the virtual force is estimated by using the difference between the prescribed solid velocity and the computed one weighted with a volume-of-solid function η to avoid the rather complicated interpolation process as that of [17,30], where the computed velocity is obtained by applying the projection scheme to the incompressible Navier–Stokes equations on the entire domain including the portion occupied by the solid body. In fact, the function η denotes the volume fraction of solid within a cell, where η equals to 1 for solid cells and 0 for fluid cells, and is fractional on cells cut by immersed boundary. However, for making the scheme as simple as possible for moving solid objects, they ignored the fractional value of η. That is, in [48], the values of η is either 1 or 0 only. In the review process of this paper, one of the reviewers pointed out the earlier work of Kajishima et al. [27,28] to us. We have found that the numerical method proposed in [27,28] is essentially identical to that of [48] for solving fluid-solid interaction problems.

Although the direct-forcing IB method proposed in [27,28,48] has been successfully applied to several engineering applications [5–7] and it seems to produce reasonable results for simulating fluid-solid interaction problems, we find that this method is not always convergent when it is combined with an inappropriate projection scheme. The main reason for this failure is due to the inconsistency between velocity and pressure at the end of each time step with velocity corrected but not pressure in the immersed solid domain. This particularly causes a problem in calculating the intermediate velocity of the next time step when employing pressure from the previous time step in the momentum equations. We will give a more detailed description of the possible inconsistency in the method in Section 2 below. This is an important finding in the present study regarding the primitive direct-forcing IB method in [27,28,48].

Motivated by the above finding, in this paper, we will provide a remedy to prevent the possible inconsistency arising in the primitive direct-forcing IB method of [27,28,48]. We will propose a simple and novel PC approach combined with the projection scheme of Choi and Moin [9], which is a second-order scheme in time, to simulate the dynamics of fluid-solid interaction problems, where each immersed solid object can be stationary or moving in the fluid with a prescribed velocity. This approach can be categorized as a direct-forcing IB projection method with a PC process. A time-discrete virtual force distributed only on the immersed solid body is introduced and added to the fluid momentum equations to accommodate the internal boundary condition at the immersed solid boundary as done in Noor et al. [48] and Kajishima et al. [27,28]. More specifically, in the prediction stage, the virtual force can be first predicted by using the difference between the prescribed solid velocity and the computed one, which is obtained by the Choi–Moin projection scheme on the entire domain without particularly considering the immersed solid object. In the correction stage, the obtained predicted virtual force is then appended to the momentum equations as an additional forcing term for calculating the intermediate velocity. We then perform the Choi–Moin projection again to update the velocity and pressure fields, and correct the velocity in immersed solid domain to obtain the corrected virtual force. Although this direct-forcing IB projection method with PC is a two-stage approach, the computational cost of the correction stage is rather cheap, since the associated discrete linear systems need to be solved in the correction stage are same with that in the prediction stage, except the right-hand side data terms. Apparently, such a PC procedure can be iterated to form a more general $P(C)^k$ method for $k \geq 2$, if necessary. This two-stage method also has the advantage over the most direct-forcing IB projection methods like Noor et al. [48] and Kajishima et al. [27,28], since those direct-forcing methods are generally one-stage, which request quite small
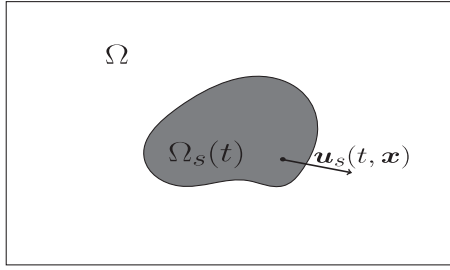
Fig. 2.1. A schematic diagram of flow over a moving solid body $\overline{\Omega}_s(t)$ at time t.

Fig. 3.1. A schematic diagram of the 2-D computational domain Ω with staggered grid, where the unknowns u, v and p are approximated at the grid points marked by $\rightarrow$, $\uparrow$ and $\bullet$, respectively.

time step for flow field relaxed and adjusted to the solid body movement even using implicit scheme.

In this paper, we will perform numerical experiments of several fluid-solid interaction problems to illustrate the simplicity and efficient performance of this newly proposed approach, including the flow induced by a rotating cylinder inside a square enclosure for convergence test, the flow past a stationary cylinder, the flow past an in-line oscillating cylinder, and the flow induced by two cylinders moving towards each other. All these numerical examples show the high capability of this newly proposed method in solving complex-geometry flow problems. In particular, we find from the convergence test that the order of convergence of the velocity field is super-linear in space in 1-norm, 2-norm, and maximum norm, while the pressure is only first-order accurate in 1-norm and 2-norm and somewhat nearly half-order accurate in the maximum norm. We also find that our numerical results are in very good agreement with the previous works in the literature and one correction at each time step appears to be good enough for the proposed PC procedure. Finally, to validate the ability of the proposed method for solving two-way fluid-solid interaction problems in which the velocity of each immersed solid object is not prescribed, promising numerical results of the free-falling process of a 2-D solid ball are presented.

In summary, the main contributions of this paper are twofold. First, we clearly describe how the inconsistency problem might arise in the primitive direct-forcing IB method [27,28,48]. The second contribution is that we devise a two-stage direct-forcing method successfully preventing the possible inconsistency and efficiently simulating the dynamics of fluid-solid interaction problems.

The remainder of this paper is organized as follows. In Section 2, we demonstrate how the possible inconsistency arises in the primitive direct-forcing IB projection method when the projection scheme adopted in the method is not carefully chosen. In Section 3, we introduce the new and simple direct-forcing IB projection method with a PC process. Numerical experiments for several benchmark problems are presented in Section 4. Finally, a brief summary and conclusions are given in Section 5.

2. A primitive direct-forcing IB projection method and the inconsistency

Let $\Omega \subset \mathbb{R}^d$, $d = 2$ or 3, be a bounded fluid domain which encloses, for simplicity, a single rigid solid body positioned at $\overline{\Omega}_s(t)$ with the prescribed velocity $\boldsymbol{u}_s$, see Fig. 2.1. One of the Cartesian grid based non-boundary conforming methods for efficiently simulating fluid-solid interaction problems is the direct-forcing IB method of Noor et al. [48] and Kajishima et al. [27,28], in which the solid part is treated like a fluid but with an additional virtual force field $\boldsymbol{F}$ applied only to the solid portion so that it would behave like a real solid body. In practice, this virtual force $\boldsymbol{F}$ is added to the momentum equations to accommodate the interaction between the solid and fluid such that the internal boundary condition at the immersed solid boundary is exactly satisfied. Thus the
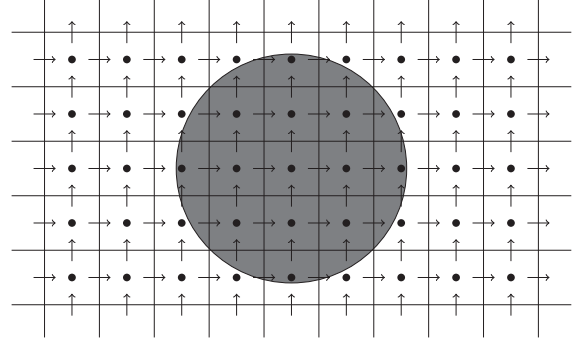
problem can be solved on the entire domain Ω with a Cartesian grid. Of course, how to find the virtual force $\boldsymbol{F}$ is the most crucial issue. Later we will specify such virtual force in its time-discrete version in the projection computations. At this moment, the governing equations of the dynamics of the fluid-solid interaction can be informally posed as follows:

$$\frac{\partial \boldsymbol{u}}{\partial t} - \nu \nabla^2 \boldsymbol{u} + (\boldsymbol{u} \cdot \nabla)\boldsymbol{u} + \nabla p = \boldsymbol{f} + \boldsymbol{F} \quad t \in (0, T], \quad \boldsymbol{x} \in \Omega, \quad (2.1)$$

$$\nabla \cdot \boldsymbol{u} = 0 \quad t \in (0, T], \quad \boldsymbol{x} \in \Omega, \quad (2.2)$$

$$\boldsymbol{u} = \boldsymbol{u}_b \quad t \in (0, T], \quad \boldsymbol{x} \in \partial\Omega, \quad (2.3)$$

$$\boldsymbol{u} = \boldsymbol{u}_0 \quad t = 0, \quad \boldsymbol{x} \in \overline{\Omega}, \quad (2.4)$$

where $\boldsymbol{u}$ is the velocity field, p is the pressure (divided by a constant density ρ), ν is the kinematic viscosity, and $\boldsymbol{f}$ represents the density of body force.

To introduce the direct-forcing IB projection approach of Noor et al. [48] and Kajishima et al. [27,28], we first discretize the temporal variable t of the incompressible Navier–Stokes problem (2.1)–(2.4), with the spatial variable $\boldsymbol{x}$ being left continuous. Let $t_i := i\Delta t$ with $\Delta t > 0$ be the time step length. Let $\boldsymbol{g}^n$ and $\boldsymbol{g}^{n+\frac{1}{2}}$ denote the approximate value or exact value (if available) of $\boldsymbol{g}(t_n)$ and $\boldsymbol{g}(t_{n+\frac{1}{2}})$, respectively. The temporal integration of (2.1)–(2.4) is based on a semi-implicit second-order difference method, in which the Crank–Nicolson implicit scheme will be employed for time discretization, the Adams–Bashforth explicit approximation will be used for linearizing the nonlinear convection term, and a direct second-order approximation will be applied to both the pressure and the virtual force. More specifically, we use the following temporal approximations:

$$\frac{1}{2}\big((\boldsymbol{u}^{n+1} \cdot \nabla)\boldsymbol{u}^{n+1} + (\boldsymbol{u}^n \cdot \nabla)\boldsymbol{u}^n\big) = \frac{3}{2}(\boldsymbol{u}^n \cdot \nabla)\boldsymbol{u}^n - \frac{1}{2}(\boldsymbol{u}^{n-1} \cdot \nabla)\boldsymbol{u}^{n-1} + O(\Delta t^2), \quad (2.5)$$

$$\frac{1}{2}\big(\nabla p^{n+1} + \nabla p^n\big) = \nabla p^{n+\frac{1}{2}} + O(\Delta t^2) \quad \text{and}$$

$$\frac{1}{2}\big(\boldsymbol{F}^{n+1} + \boldsymbol{F}^n\big) = \boldsymbol{F}^{n+\frac{1}{2}} + O(\Delta t^2). \quad (2.6)$$

With these second-order approximations, the resulting system of equations can be posed as follows:

$$\frac{\boldsymbol{u}^{n+1} - \boldsymbol{u}^n}{\Delta t} - \frac{\nu}{2}\nabla^2(\boldsymbol{u}^{n+1} + \boldsymbol{u}^n) + \frac{3}{2}(\boldsymbol{u}^n \cdot \nabla)\boldsymbol{u}^n$$

Table 4.1
Error behavior of the numerical solutions u_h, v_h and p_h of the rotating solid disk problem at time $T = 4$ using the numerical solution of $h = 1/1620$ as the reference solution.

	$1/h$	1-norm	Order	2-norm	Order	Max-norm	Order
u_h	20	2.0820e−02	–	3.9742e−02	–	1.7573e−01	–
	60	8.4854e−03	0.82	1.7044e−02	0.77	8.2900e−02	0.68
	180	2.5123e−03	1.11	5.0608e−03	1.11	2.8370e−02	0.98
	540	6.5240e−04	1.23	1.3207e−03	1.22	8.1061e−03	1.14
v_h	20	2.5334e−02	–	4.2845e−02	–	1.7573e−01	–
	60	1.0199e−02	0.83	1.8496e−02	0.76	8.2900e−02	0.68
	180	3.0741e−03	1.09	5.5503e−03	1.10	2.8554e−02	0.97
	540	7.9659e−04	1.23	1.4500e−03	1.22	8.1061e−03	1.15
p_h	20	6.8326e−03	–	1.3968e−02	–	8.4475e−02	–
	60	3.0749e−03	0.73	6.2523e−03	0.73	4.8072e−02	0.51
	180	9.8066e−04	1.04	2.1771e−03	0.96	3.8831e−02	0.19
	540	2.6861e−04	1.18	7.5445e−04	0.96	2.5701e−02	0.38

Table 4.2
The comparison of experimental and numerical results of steady state wake dimensions and maximum drag coefficient of the flow around a stationary cylinder for $Re = 20, 40$.

Reynolds number	20					40				
Methods	C_d	L_w/D	a/D	b/D	θ	C_d	L_w/D	a/D	b/D	θ
Calhoun [4]	2.19	0.91	–	–	45.5	1.62	2.18	–	–	54.2
Coutanceau and Bouard* [14]	–	0.93	0.33	0.46	45.0	–	2.13	0.76	0.59	53.8
Linnick and Fasel [42]	2.06	0.93	0.36	0.43	43.5	1.54	2.28	0.72	0.60	53.6
Su et al. [54]	2.20	–	–	–	–	1.63	–	–	–	–
Taira and Colonius (B) [55]	2.06	0.94	0.37	0.43	43.3	1.54	2.30	0.73	0.60	53.7
Tritton* [57]	2.22	–	–	–	–	1.48	–	–	–	–
Ye et al. [66]	2.03	0.92	–	–	–	1.52	2.27	–	–	–
Present method-P	2.12	0.92	0.36	0.42	44.6	1.59	2.20	0.71	0.60	51.2
Present method-PC	2.10	0.93	0.35	0.43	43.5	1.56	2.18	0.72	0.60	53.3
Present method-PCC	2.09	0.93	0.35	0.44	44.1	1.54	2.18	0.71	0.60	53.0
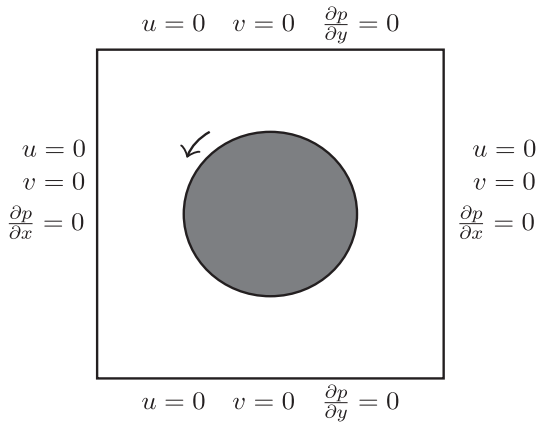
Fig. 4.1. Boundary conditions of the problem of flow induced by a rotating solid disk.

$$-\frac{1}{2}(\boldsymbol{u}^{n-1} \cdot \nabla)\boldsymbol{u}^{n-1} + \nabla p^{n+\frac{1}{2}} = [\boldsymbol{f}]^{n+\frac{1}{2}} + \boldsymbol{F}^{n+\frac{1}{2}} \quad \text{in } \Omega, \qquad (2.7)$$

$$\nabla \cdot \boldsymbol{u}^{n+1} = 0 \quad \text{in } \Omega, \qquad (2.8)$$

$$\boldsymbol{u}^{n+1} = \boldsymbol{u}_b^{n+1} \quad \text{on } \partial\Omega, \qquad (2.9)$$

where $[\boldsymbol{f}]^{n+\frac{1}{2}}$ denotes the average value of the density of body force $\frac{1}{2}(\boldsymbol{f}^{n+1} + \boldsymbol{f}^n)$. Obviously, it is not an efficient way to solve this linearized coupled system of Stokes-like equations directly. This is precisely the reason for proposing the projection approach to decouple the computations of $\boldsymbol{u}^{n+1}$ and $p^{n+\frac{1}{2}}$.

We now introduce the primitive direct-forcing IB projection method which was proposed by Noor et al. [48] and Kajishima

et al. [27,28] for solving system (2.7)–(2.9). In this section, we will replace the first-order in time Chorin projection scheme [11,12] originally adopted in [27,28,48] by the second-order in time projection scheme of Brown et al. [3]. This will enable us to understand how the inconsistency may possibly arise and cause convergence problem in the direct-forcing IB projection approach if not selecting projection scheme appropriately. At the beginning of time level $t = t_{n+1}$, the velocities $\boldsymbol{u}^n$, $\boldsymbol{u}^{n-1}$, the pressure $p^{n-\frac{1}{2}}$ and the density of body force $[\boldsymbol{f}]^{n+\frac{1}{2}}$ are all given. The numerical scheme consists of the following several steps:

Step 1: First, we solve $\boldsymbol{u}^*$ without virtual force term for the momentum equations:

$$\frac{\boldsymbol{u}^* - \boldsymbol{u}^n}{\Delta t} - \frac{\nu}{2}\nabla^2(\boldsymbol{u}^* + \boldsymbol{u}^n) + [(\boldsymbol{u} \cdot \nabla)\boldsymbol{u}]^{n+\frac{1}{2}} + \nabla p^{n-\frac{1}{2}} = [\boldsymbol{f}]^{n+\frac{1}{2}} \quad \text{in } \Omega, \qquad (2.10)$$

$$\boldsymbol{u}^* = \boldsymbol{u}_b^{n+1} \quad \text{on } \partial\Omega, \qquad (2.11)$$

where $[(\boldsymbol{u} \cdot \nabla)\boldsymbol{u}]^{n+\frac{1}{2}}$ denotes the Adams–Bashforth second-order approximation given in (2.5), i.e.,

$$[(\boldsymbol{u} \cdot \nabla)\boldsymbol{u}]^{n+\frac{1}{2}} := \frac{3}{2}(\boldsymbol{u}^n \cdot \nabla)\boldsymbol{u}^n - \frac{1}{2}(\boldsymbol{u}^{n-1} \cdot \nabla)\boldsymbol{u}^{n-1}. \qquad (2.12)$$

We remark that in general, the intermediate velocity field $\boldsymbol{u}^*$ does not satisfy the divergence-free condition in Ω.

Step 2: In this step, we will advance the intermediate velocity $\boldsymbol{u}^*$ by using the pressure correction function φ^{n+1}. The role that φ^{n+1} plays is an auxiliary function whose main purpose is to project $\boldsymbol{u}^*$. Indeed, we determine $\boldsymbol{u}^{**}$ and φ^{n+1} by solving

$$\frac{\boldsymbol{u}^{**} - \boldsymbol{u}^*}{\Delta t} + \nabla \varphi^{n+1} = \boldsymbol{0} \quad \text{in } \Omega, \qquad (2.13)$$
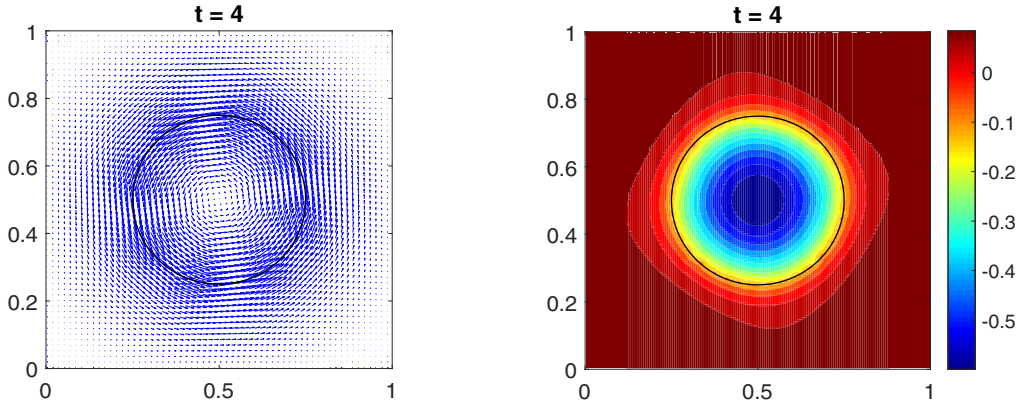
Fig. 4.2. Numerical results of the velocity field and pressure contours of the rotating solid disk problem at time $t = 4$ produced by the present method with $h = 1/180$.
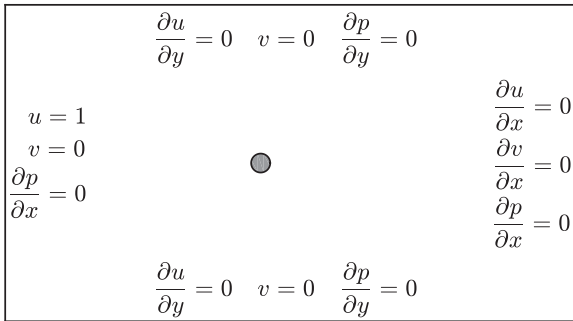
Fig. 4.3. Boundary conditions of the problem of flow past a cylinder.

$$\nabla \cdot \boldsymbol{u}^{**} = 0 \quad \text{in } \Omega, \tag{2.14}$$

$$\boldsymbol{u}^{**} \cdot \boldsymbol{n} = \boldsymbol{u}_b^{n+1} \cdot \boldsymbol{n} \quad \text{on } \partial\Omega. \tag{2.15}$$

The existence and uniqueness (up to a constant for φ^{n+1}) of solution of the above boundary value problem (2.13)–(2.15) is ensured by the Helmholtz–Hodge decomposition [13]. In fact, taking the divergence to (2.13), dotting both sides of (2.13) with the outward unit normal vector $\boldsymbol{n}$ to the boundary $\partial\Omega$, and combining with the boundary conditions (2.11) and (2.15), we can find that solving system (2.13)–(2.15) is equivalent to solve the following φ^{n+1}-Neumann Poisson problem:

$$\nabla^2 \varphi^{n+1} = \frac{1}{\Delta t} \nabla \cdot \boldsymbol{u}^* \quad \text{in } \Omega, \tag{2.16}$$

$$\nabla \varphi^{n+1} \cdot \boldsymbol{n} = 0 \quad \text{on } \partial\Omega, \tag{2.17}$$

and then define the velocity field $\boldsymbol{u}^{**}$ as

$$\boldsymbol{u}^{**} = \boldsymbol{u}^* - \Delta t \nabla \varphi^{n+1} \quad \text{in } \Omega. \tag{2.18}$$

In practical computations, we usually impose the condition $\int_\Omega \varphi^{n+1} d\boldsymbol{x} = 0$ to the Neumann Poisson problem (2.16)–(2.17) for the uniqueness of solution.

Step 3: Conventionally, (2.18) would be the end of projection scheme for finding the velocity field and we have to set $\boldsymbol{u}^{n+1} = \boldsymbol{u}^{**}$; see, e.g., [1,11,12,20,21,31,56,58,69]. However, in order to make the velocity of solid domain to cope with prescribed solid body velocity, we need an additional step to reset the velocity of solid domain to be the same as that of the solidâs velocity $\boldsymbol{u}_s^{n+1}$. This would naturally make

the fluid satisfy the internal boundary condition at the immersed solid boundary $\partial\Omega_s^{n+1}$. This can be accomplished by defining the virtual force on the solid body as

$$\boldsymbol{F}^{n+\frac{1}{2}} := \eta \frac{\boldsymbol{u}_s^{n+1} - \boldsymbol{u}^{**}}{\Delta t} \quad \text{on } \overline{\Omega}, \tag{2.19}$$

and then solve the velocity $\boldsymbol{u}^{n+1}$ by directly setting

$$\frac{\boldsymbol{u}^{n+1} - \boldsymbol{u}^{**}}{\Delta t} = \boldsymbol{F}^{n+\frac{1}{2}} \quad \text{in } \Omega, \tag{2.20}$$

where $\eta(t_{n+1}, \boldsymbol{x})$ is defined as

$$\eta(t_{n+1}, \boldsymbol{x}) = \begin{cases} 1 & \boldsymbol{x} \in \overline{\Omega}_s^{n+1}, \\ 0 & \boldsymbol{x} \notin \overline{\Omega}_s^{n+1}. \end{cases} \tag{2.21}$$

Note that the virtual force $\boldsymbol{F}^{n+\frac{1}{2}}$ exists on the whole solid body and zero elsewhere. In other words, in this step, we simply set

$$\boldsymbol{u}^{n+1} = \begin{cases} \boldsymbol{u}^{**} & \text{in } \overline{\Omega} \setminus \overline{\Omega}_s^{n+1}, \\ \boldsymbol{u}_s^{n+1} & \text{in } \overline{\Omega}_s^{n+1}. \end{cases} \tag{2.22}$$

We remark that in the spatial discretization that will be specified in Section 4, the function η denotes the volume fraction of solid inside a cell and it is generally between 0 (pure fluid) and 1 (pure solid) and can be fractional for cells cut by immersed solid boundary.

Step 4: Finally, summing the equations (2.10), (2.13), (2.20) with (2.18), we obtain

$$\frac{\boldsymbol{u}^{n+1} - \boldsymbol{u}^n}{\Delta t} - \frac{\nu}{2} \nabla^2 (\boldsymbol{u}^{**} + \boldsymbol{u}^n) + [(\boldsymbol{u} \cdot \nabla)\boldsymbol{u}]^{n+\frac{1}{2}}$$
$$+ \nabla \left(p^{n-\frac{1}{2}} + \varphi^{n+1} - \frac{\nu \Delta t}{2} \nabla^2 \varphi^{n+1} \right) = [\boldsymbol{f}]^{n+\frac{1}{2}} + \boldsymbol{F}^{n+\frac{1}{2}} \quad \text{in } \Omega, \tag{2.23}$$

which comparing with (2.7) suggests that in this last step of the projection scheme, we should update the pressure by setting

$$p^{n+\frac{1}{2}} := p^{n-\frac{1}{2}} + \varphi^{n+1} - \frac{\nu \Delta t}{2} \nabla^2 \varphi^{n+1} \quad \text{in } \Omega. \tag{2.24}$$

The above direct-forcing IB projection method is simply formed by combining the second-order in time projection scheme of Brown et al. [3] with the underlying idea of the direct-forcing approach proposed by Noor et al. [48] and Kajishima et al. [27,28]. It seems to be a reasonable scheme for solving fluid-solid interaction problems. However, based on our numerical experiments, we find that in general it does not converge for the 2-D problem of flow
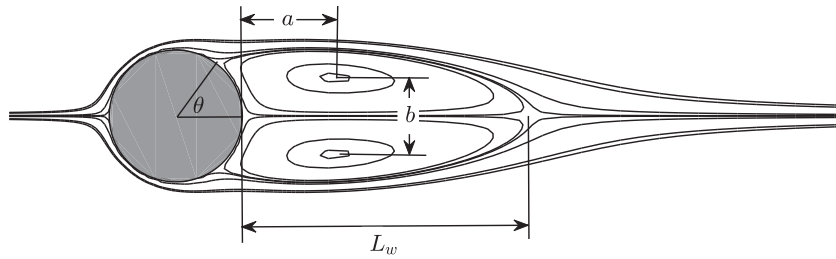
Fig. 4.4. The characteristic dimensions of wake structure.
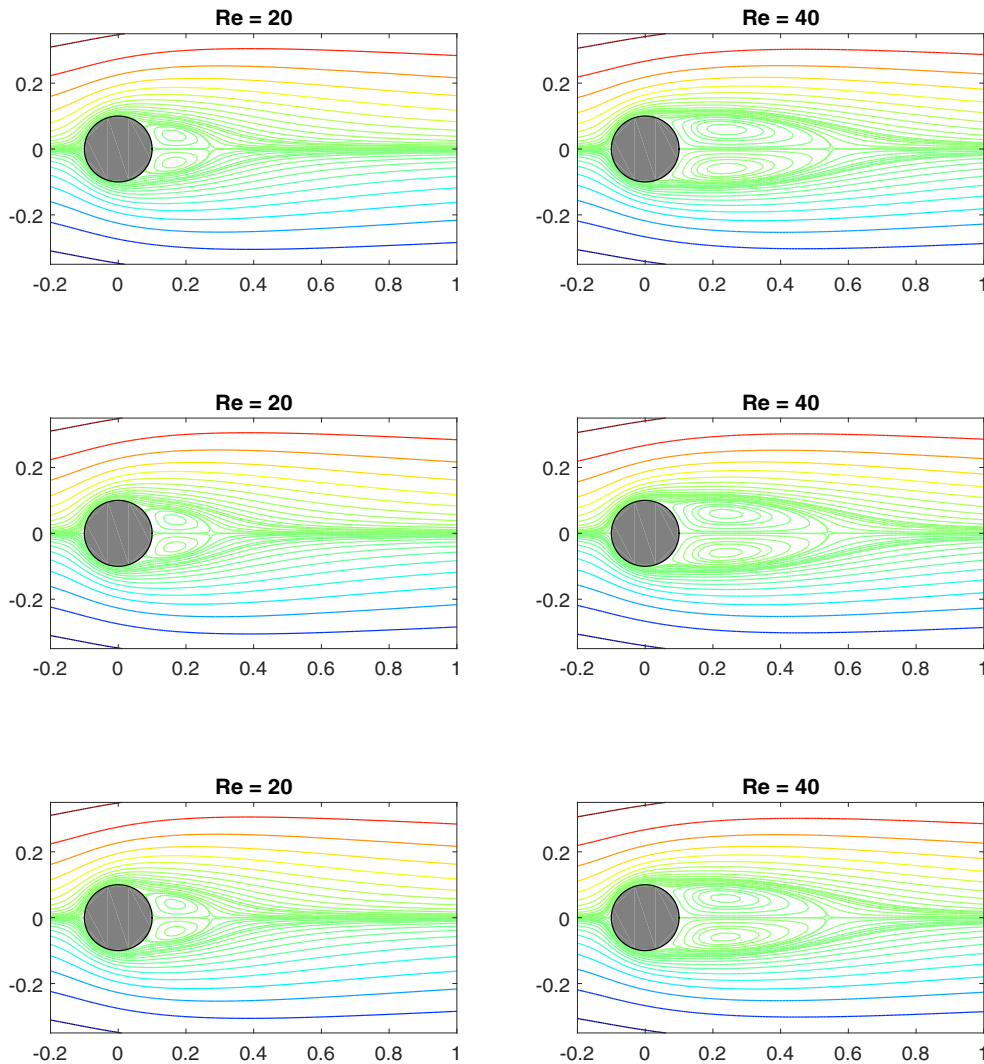
Fig. 4.5. The instantaneous streamlines near the cylinder at time $T = 50$ for $Re = 20$ and $Re = 40$ (top to bottom: present method-P, present method-PC, and present method-PCC).

past a stationary cylinder, unless the time step is very small. The reason for this failure is because that in the projection computations, the obtained velocity field $\boldsymbol{u}^{n+1}$ and pressure $p^{n+\frac{1}{2}}$ at current time level $t = t_{n+1}$, which will be used in solving the intermediate velocity field $\boldsymbol{u}^*$ in the next time level $t = t_{n+2}$, may not be consistent. More precisely, we can find that the velocity $\boldsymbol{u}^{n+1}$ is directly obtained by setting (2.22) that is identical to $\boldsymbol{u}^{**}$ in the fluid part, but is enforced to be $\boldsymbol{u}_s^{n+1}$ in the solid part. At the same time, however, the pressure $p^{n+\frac{1}{2}}$ is obtained by (2.24) which is essentially determined along with the velocity field $\boldsymbol{u}^{**}$ in Step 2. In other words, $p^{n+\frac{1}{2}}$ is consistent with $\boldsymbol{u}^{**}$ but not $\boldsymbol{u}^{n+1}$. Therefore, the in-

consistency may arise in the next time level $t = t_{n+2}$ when we perform Step 1 for the intermediate velocity $\boldsymbol{u}^*$ by solving (2.10) and (2.11), where, at this moment, $\boldsymbol{u}^n$ should be replaced by $\boldsymbol{u}^{n+1}$ and $p^{n-\frac{1}{2}}$ replaced by $p^{n+\frac{1}{2}}$. We can therefore conclude that a careful choice of projection scheme plays a crucial role for the success of such direct-forcing IB projection approach. This critical observation is one of the main contributions of this work and it motivates us to seek the necessary improvements.

We remark that the choice of first-order in time Chorin projection scheme in Noor et al. [48] and Kajishima et al. [27,28] luckily avoid the inconsistency, since there would be no pressure term in
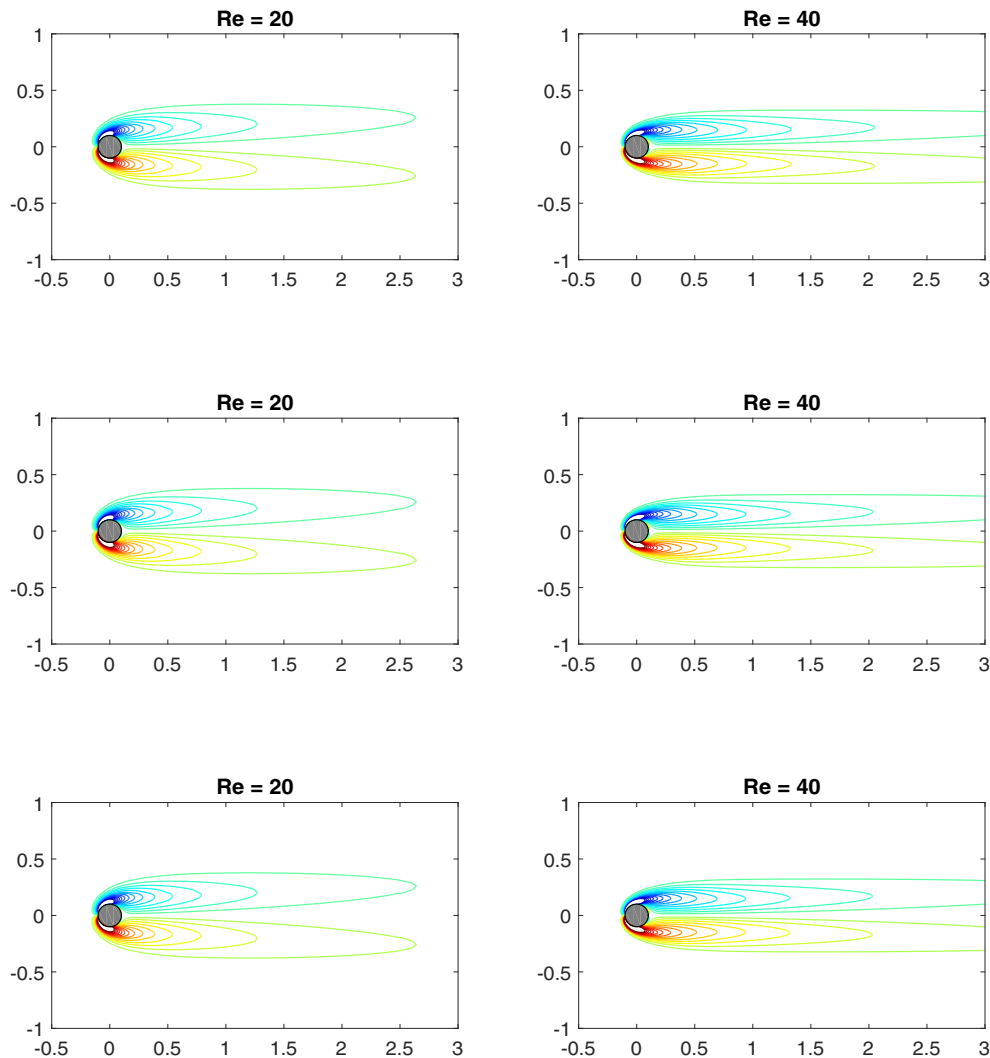
Fig. 4.6. The instantaneous vorticity contours near the cylinder at time $T = 50$ for $Re = 20$ and $Re = 40$ (top to bottom: present method-P, present method-PC, and present method-PCC).

solving the intermediate velocity $\boldsymbol{u}^*$. Still, there are other projection schemes can avoid this inconsistency and at the same time own higher-order accuracy in time such as the Choi–Moin second-order projection scheme [9]. In the next section, we will provide a far better remedy to retrieve the time accuracy of the direct-forcing IB projection method. We will propose a simple and novel PC approach, combined with the second-order in time projection scheme of Choi and Moin [9], to simulate the dynamics of fluid-solid interaction problems. This is another main contribution of this work. The results of the numerical experiments reported in Section 4 will demonstrate the efficiency and robustness of the proposed prediction-correction strategy.

There are several similar direct-forcing IB methods have been proposed and studied in the literature, see e.g., [2,15,17,22,26,29,40,44,59,61,64,67,68]. Generally speaking, in those methods the forcing term $\boldsymbol{F}$ appended to the momentum equations due to the presence of solid body has to be determined at the advanced time level before the solution procedure can be started. Moreover, this momentum forcing is located only in a neighborhood of the immersed solid boundary. As a result, the immersed boundary condition on $\partial\Omega_s$ can only be approximately satisfied, while the velocity field is divergence free on the whole spatial domain Ω. In contrast, the virtual force in the direct-forcing method of Noor et al. [48] and Kajishima et al. [27,28] is defined

on the whole solid body domain as that specified in (2.19). Such virtual force does not need to be estimated at the beginning of the solution procedure, it is explicitly determined after the velocity field $\boldsymbol{u}^{**}$ is obtained. That is, the step of determination of virtual force (Step 3) is implemented after the projection step (Step 2). This leads the immersed boundary condition to be exactly satisfied. However, the divergence-free condition may be destroyed in cut cells at which the solid-fluid interface is located. More of this divergence-free issue will be discussed in Section 4.2. These are the main differences between the direct-forcing IB method of Noor et al. [48] and Kajishima et al. [27,28] with other previous direct-forcing IB methods in the literature.

3. A direct-forcing IB projection method with a prediction-correction process

In this section, we will propose a simple and novel direct-forcing IB projection method with a PC process, where the second-order in time Choi–Moin projection scheme [9] will be employed for the time discretization. The main idea of this approach is based on using a PC strategy to enhance the consistency of the primitive method. The proposed method is divided into following two stages:
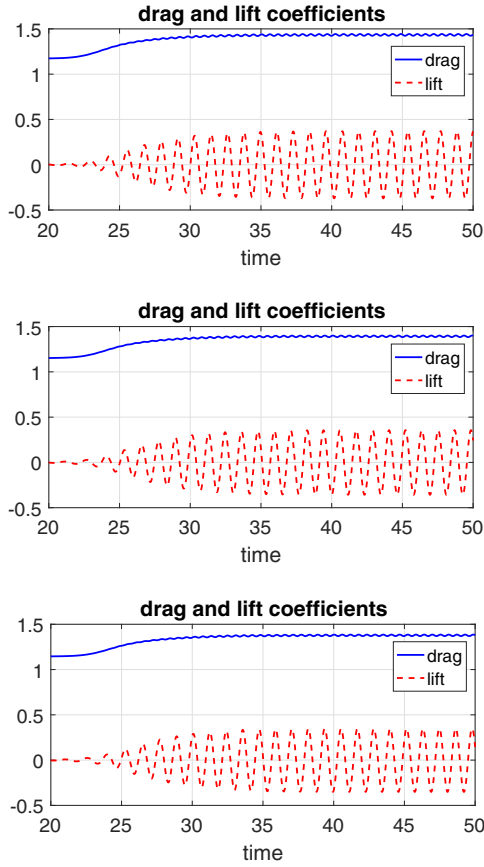
Fig. 4.7. The time evolution of drag and lift coefficients for $Re = 100$ (top to bottom: present method-P, present method-PC, and present method-PCC).

- *Prediction stage:* In this stage, we predict the virtual force $\boldsymbol{F}^{n+\frac{1}{2},p}$ by using the primitive direct-forcing IB projection approach as that described in Section 2. All unknown variables are equipped with the superscript "p" to indicate that they are unknown functions to be solved in this stage. Firstly, we solve $\boldsymbol{u}^{*,p}$ without virtual force term for the momentum equations:

$$\frac{\widetilde{\boldsymbol{u}}^p - \boldsymbol{u}^n}{\Delta t} - \frac{\nu}{2}\nabla^2(\widetilde{\boldsymbol{u}}^p + \boldsymbol{u}^n) + [(\boldsymbol{u}\cdot\nabla)\boldsymbol{u}]^{n+\frac{1}{2}} + \nabla p^{n-\frac{1}{2}} =$$
$$[\boldsymbol{f}]^{n+\frac{1}{2}} \quad \text{in } \Omega, \tag{3.1}$$

$$\widetilde{\boldsymbol{u}}^p = \boldsymbol{u}_b^{n+1} \quad \text{on } \partial\Omega, \tag{3.2}$$

$$\frac{\boldsymbol{u}^{*,p} - \widetilde{\boldsymbol{u}}^p}{\Delta t} - \nabla p^{n-\frac{1}{2}} = \boldsymbol{0} \quad \text{in } \Omega, \tag{3.3}$$

where $\widetilde{\boldsymbol{u}}^p$ is another tentative velocity field which is introduced for avoiding any special treatment of the boundary condition of intermediate velocity $\boldsymbol{u}^{*,p}$ and for keeping the overall accuracy of the projection scheme to be second-order accurate in time; we refer the reader to [9,31] for more details. Notice that in general, the intermediate velocity field $\boldsymbol{u}^{*,p}$ does not satisfy the divergence-free condition in Ω. Secondly, we advance the intermediate velocity $\boldsymbol{u}^{*,p}$ by using the pressure correction function $\varphi^{n+1,p}$. We determine $\boldsymbol{u}^{**,p}$ and $\varphi^{n+1,p}$ by solving

$$\frac{\boldsymbol{u}^{**,p} - \boldsymbol{u}^{*,p}}{\Delta t} + \nabla\varphi^{n+1,p} = \boldsymbol{0} \quad \text{in } \Omega, \tag{3.4}$$

$$\nabla\cdot\boldsymbol{u}^{**,p} = 0 \quad \text{in } \Omega, \tag{3.5}$$

Table 4.3
The comparison of maximum drag and lift coefficients and Strouhal number of the flow around a stationary cylinder for $Re = 100$.

Reynolds number	100		
Methods	C_d	C_ℓ	St
Calhoun [4]	1.36	0.30	0.175
Chiu et at. [8]	1.36	0.30	0.167
Lai and Peskin [36]	1.45	0.33	0.165
Liu et al. [43]	1.36	0.34	0.164
Russell and Wang [51]	1.39	0.32	0.170
Su et al. [54]	1.40	0.34	0.168
Present method-P	1.43	0.37	0.171
Present method-PC	1.40	0.36	0.170
Present method-PCC	1.38	0.35	0.168

$$\boldsymbol{u}^{**,p}\cdot\boldsymbol{n} = \boldsymbol{u}_b^{n+1}\cdot\boldsymbol{n} \quad \text{on } \partial\Omega, \tag{3.6}$$

which is equivalent to solve the $\varphi^{n+1,p}$-Neumann Poisson problem,

$$\nabla^2\varphi^{n+1,p} = \frac{1}{\Delta t}\nabla\cdot\boldsymbol{u}^{*,p} \quad \text{in } \Omega, \tag{3.7}$$

$$\nabla\varphi^{n+1,p}\cdot\boldsymbol{n} = 0 \quad \text{on } \partial\Omega, \tag{3.8}$$

and then define the velocity field $\boldsymbol{u}^{**,p}$ as

$$\boldsymbol{u}^{**,p} = \boldsymbol{u}^{*,p} - \Delta t\nabla\varphi^{n+1,p} \quad \text{in } \Omega. \tag{3.9}$$

The additional condition $\int_\Omega \varphi^{n+1,p}d\boldsymbol{x} = 0$ is imposed to the Neumann Poisson problem (3.7)–(3.8) for the uniqueness of solution. Finally, we predict the virtual force $\boldsymbol{F}^{n+\frac{1}{2},p}$ by setting

$$\boldsymbol{F}^{n+\frac{1}{2},p} := \eta\frac{\boldsymbol{u}_s^{n+1} - \boldsymbol{u}^{**,p}}{\Delta t} \quad \text{on } \overline{\Omega}, \tag{3.10}$$

where $\eta(t_{n+1},\boldsymbol{x}) = 1$ for $\boldsymbol{x}\in\overline{\Omega}_s^{n+1}$ and $\eta(t_{n+1},\boldsymbol{x}) = 0$ for $\boldsymbol{x}\notin\overline{\Omega}_s^{n+1}$.

- *Correction stage:* Once the predicted virtual force $\boldsymbol{F}^{n+\frac{1}{2},p}$ is obtained, in this stage, we then add it to the right-hand side of (3.1) as an additional forcing term and find the new intermediate velocity field $\boldsymbol{u}^*$. With this predicted virtual force $\boldsymbol{F}^{n+\frac{1}{2},p}$, the immersed solid object can be immediately felt by the fluid occupying the same domain and make it act more like a solid object. More precisely, we solve for $\boldsymbol{u}^*$ by

$$\frac{\widetilde{\boldsymbol{u}} - \boldsymbol{u}^n}{\Delta t} - \frac{\nu}{2}\nabla^2(\widetilde{\boldsymbol{u}} + \boldsymbol{u}^n) + [(\boldsymbol{u}\cdot\nabla)\boldsymbol{u}]^{n+\frac{1}{2}} + \nabla p^{n-\frac{1}{2}} =$$
$$[\boldsymbol{f}]^{n+\frac{1}{2}} + \boldsymbol{F}^{n+\frac{1}{2},p} \quad \text{in } \Omega, \tag{3.11}$$

$$\widetilde{\boldsymbol{u}} = \boldsymbol{u}_b^{n+1} \quad \text{on } \partial\Omega, \tag{3.12}$$

$$\frac{\boldsymbol{u}^* - \widetilde{\boldsymbol{u}}}{\Delta t} - \nabla p^{n-\frac{1}{2}} = \boldsymbol{0} \quad \text{in } \Omega. \tag{3.13}$$

Then solve for the pressure correction function φ^{n+1} by

$$\nabla^2\varphi^{n+1} = \frac{1}{\Delta t}\nabla\cdot\boldsymbol{u}^* \quad \text{in } \Omega, \tag{3.14}$$

$$\nabla\varphi^{n+1}\cdot\boldsymbol{n} = 0 \quad \text{on } \partial\Omega, \tag{3.15}$$

and update the velocity field $\boldsymbol{u}^{**}$ by

$$\boldsymbol{u}^{**} = \boldsymbol{u}^* - \Delta t\nabla\varphi^{n+1} \quad \text{in } \Omega \tag{3.16}$$
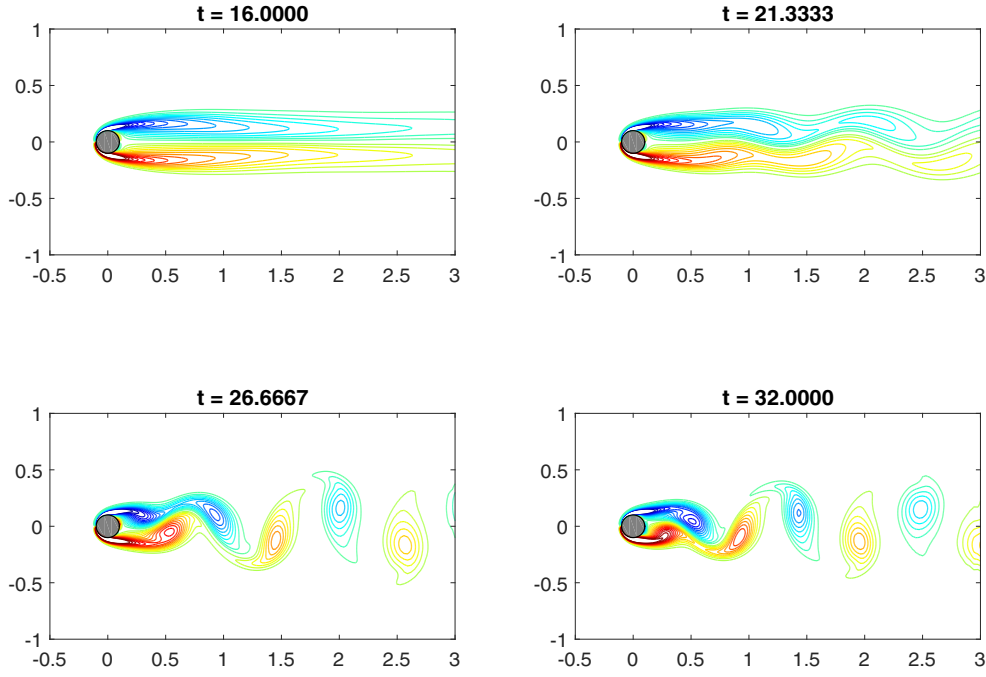
Fig. 4.8. The instantaneous vorticity contours for *Re* = 100 at different times.

Table 4.4
The computational domain $\overline{\Omega}$, diameter *D* and center of the circular cylinder of some methods quoted in Table 4.2 and 4.3.

Methods	Computational domain $\overline{\Omega}$	Diameter *D*	Center
Calhoun [4]	$[0, 32D] \times [0, 16D]$	1.0	(8, 8)
Linnick and Fasel [42]	$[0, 46.5795D] \times [-21.3278D, 21.3278D]$	1.0	(10, 0)
Su et al. [54]	$[-13.4D, 16.5D] \times [-8.35D, 8.35D]$	0.2	(0, 0)
Taira and Colonius (B) [55]	$[-30D, 30D] \times [-30D, 30D]$	1.0	(0, 0)
Ye et al. [66]	$[-10D, 20D] \times [-10D, 20D]$	1.0	(5, 7.5)
Chiu et at. [8]	$[0, 40D] \times [-10D, 10D]$	1.0	(9.5, 0)
Lai and Peskin [36]	$[0, 26.6667D] \times [0, 26.6667D]$	0.3	(1.85, 4)
Russell and Wang [51]	$[-8D, 24D] \times [-8D, 8D]$	1.0	(0, 0)
Present method	$[-13.4D, 16.5D] \times [-8.35D, 8.35D]$	0.2	(0, 0)

and correct the pressure $p^{n+\frac{1}{2}}$ by

$$p^{n+\frac{1}{2}} = \varphi^{n+1} - \frac{\nu}{2}\nabla \cdot \widetilde{\boldsymbol{u}}. \tag{3.17}$$

We then define the corrected velocity field $\boldsymbol{u}^{n+1}$ as

$$\boldsymbol{u}^{n+1} := \begin{cases} \boldsymbol{u}^{**} & \text{in } \overline{\Omega} \setminus \overline{\Omega}_s^{n+1}, \\ \boldsymbol{u}_s^{n+1} & \text{in } \overline{\Omega}_s^{n+1}. \end{cases} \tag{3.18}$$

The correction term of virtual force is given by

$$\delta\boldsymbol{F}^{n+\frac{1}{2}} := \eta \frac{\boldsymbol{u}_s^{n+1} - \boldsymbol{u}^{**}}{\Delta t} \quad \text{in } \Omega, \tag{3.19}$$

and then the corrected virtual force becomes

$$\boldsymbol{F}^{n+\frac{1}{2}} = \boldsymbol{F}^{n+\frac{1}{2},p} + \delta\boldsymbol{F}^{n+\frac{1}{2}}. \tag{3.20}$$

Regarding this direct-forcing IB projection method with PC, we have following several remarks:

Remark 3.1. As we have mentioned at the end of Section 2, a careful choice of the projection schemes plays a crucial role for the success of the primitive direct-forcing IB projection approach. In this newly proposed method, we employ the second-order in time Choi–Moin projection scheme [9] and one can find from (3.1)–(3.3) and (3.11)–(3.13) that the pressure prediction term $\nabla p^{n-\frac{1}{2}}$ essentially does not appear in the first step of the computations for solving $\boldsymbol{u}^{*,p}$ and $\boldsymbol{u}^*$. For example, summing equations (3.1) and (3.3),

we get

$$\frac{\boldsymbol{u}^{*,p} - \boldsymbol{u}^n}{\Delta t} - \frac{\nu}{2}\nabla^2(\widetilde{\boldsymbol{u}}^p + \boldsymbol{u}^n) + [(\boldsymbol{u} \cdot \nabla)\boldsymbol{u}]^{n+\frac{1}{2}} = [\boldsymbol{f}]^{n+\frac{1}{2}} \quad \text{in } \Omega.$$

The pressure prediction term disappears therein and this somehow alleviates the inconsistency of the method.

Remark 3.2. Although this approach is a two-stage method, the computational cost of the correction stage is rather cheap, since the associated discrete linear systems need to be solved in the correction stage are same with that in the prediction stage, except the right-hand side data terms. To elaborate, at each time level, the newly proposed PC approach described above has to solve two Helmholtz equations of $\widetilde{\boldsymbol{u}}^p$ and $\widetilde{\boldsymbol{u}}$ for obtaining the intermediate velocities $\boldsymbol{u}^{*,p}$ and $\boldsymbol{u}^*$, respectively, and two Neumann Poisson equations for the pressure correction functions $\varphi^{n+1,p}$ and φ^{n+1}. However, for all time levels, the only difference for these Helmholtz problems is the right-hand side source terms. In other words, the matrices of the resulting linear systems are the same for all Helmholtz equations, and we do not need to reassemble the matrix at each time step. Therefore, it can efficiently solve the linear systems by using, for example, the bi-conjugate gradient stabilized (Bi-CGSTAB) iterative method with an ILU preconditioner [63]. A similar situation occurs in the Neumann Poisson equations for solving the pressure correction functions $\varphi^{n+1,p}$ and φ^{n+1}.
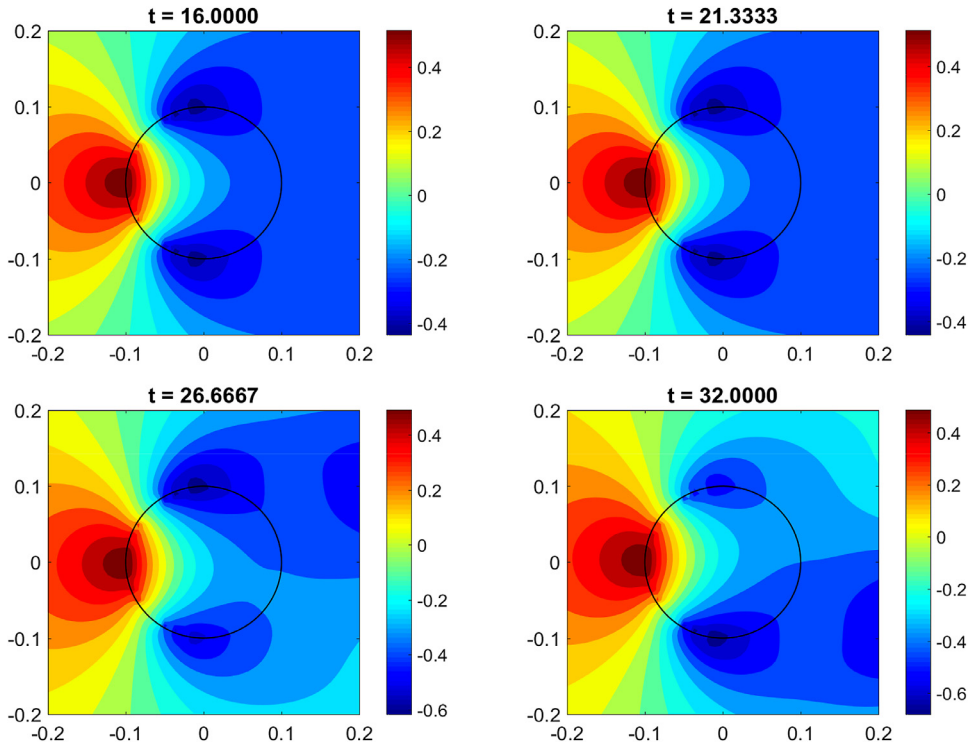
Fig. 4.9. The instantaneous pressure contours for $Re = 100$ at different times.

Remark 3.3. At each time level, such prediction-correction procedure can be iterated to form a more general method, if necessary. The stopping criterion can be taken as, for example, the L^2 norm of the difference of two successive velocity fields is less than a given tolerance. However, based on our numerical experiments, we find that at each time level, one correction appears to be good enough for the proposed PC procedure.

Finally, we conclude this section with a brief description of the spatial discretizations of the Helmholtz and Neumann Poisson problems mentioned above. For all problems, we apply the second-order centered difference scheme over a staggered grid to discretize the equations to reach a linear algebraic system. For simplicity, we assume that the computational domain is a 2-D rectangular region $\overline{\Omega} = [a, b] \times [c, d]$ and that the fluid variables are defined on the staggered marker-and-cell grids [16,23]. As shown in Fig. 3.1, we define the pressure on the grid points $(x_i, y_j) = (a + (i - 1/2)\Delta x, c + (j - 1/2)\Delta y)$ for $1 \leq i \leq m_x$ and $1 \leq j \leq m_y$, while the velocity components u and v are defined at $(x_{i-1/2}, y_j) = (a + (i - 1)\Delta x, c + (j - 1/2)\Delta y)$ for $1 \leq i \leq m_x + 1$ and $1 \leq j \leq m_y$ and $(x_i, y_{j-1/2}) = (a + (i - 1/2)\Delta x, c + (j - 1)\Delta y)$ for $1 \leq i \leq m_x$ and $1 \leq j \leq m_y + 1$, respectively. Here, we use a uniform mesh with mesh size $h = \Delta x = \Delta y$.

4. Numerical experiments

In this section, we will apply the newly proposed direct-forcing IB projection method with the PC process described in Section 3 to several 2-D fluid-solid interaction problems to illustrate the simplicity and efficient performance of the method for solving complex-geometry flow problems. We will test the accuracy of the proposed method in Section 4.1 by considering the flow induced by a rotating solid disk inside a square enclosure. In Section 4.2, we examine the flow past a stationary cylinder which is a typical benchmark problem. We then consider the moving solid objects in the fluid with a prescribed velocity in the next two

Table 4.5
The comparison of maximum lift and drag coefficients of the flow past an in-line oscillating cylinder for $Re = 100$.

$f_c/f_s = 0$	C_d	C_ℓ	$f_c/f_s = 2$	C_d	C_ℓ
Hurlbut et al. [25]	1.41	0.31	Hurlbut et al. [25]	1.68	0.95
Su et al. [54]	1.40	0.34	Su et al. [54]	1.70	0.97
Noor et al. [48]	1.41	0.33	Noor et al. [48]	1.67	0.98
Present method-PC	1.40	0.36	Present method-PC	1.67	0.98

subsections, including the flow past an in-line oscillating cylinder and the problem of two cylinders moving towards each other. The density of body force $\boldsymbol{f}$ in all the above examples is zero. In the numerical simulations, we take the volume-of-solid function $\eta = 0$ for cells of pure fluid, $\eta = 1$ for cells of pure solid and fractional for cells cut by immersed solid boundary. We find that our numerical results are in very good agreement with previous works in the literature and one correction at each time level appears to be good enough for the proposed PC procedure. Finally, in Section 4.5, we consider the free-falling process of a 2-D solid ball to validate the ability of the current method for solving two-way coupling problems.

4.1. Accuracy test for the flow induced by a rotating solid disk

In order to test the spatial convergence behavior of the direct-forcing IB projection method with the PC process, we consider the problem of flow induced by a rotating solid disk immersed in a square enclosure $\Omega = (0, 1) \times (0, 1)$, where the solid disk is centered at (0.5, 0.5) with radius $r = 0.25$ and rotates counterclockwise by a constant angular velocity $\omega = 4$, that is, $\boldsymbol{u}_s(t, x, y) = (-4(y - 0.5), 4(x - 0.5))$ for $(x, y) \in \overline{\Omega}_s$. The zero velocity boundary condition, $\boldsymbol{u} = (u, v) = (0, 0)$, is imposed everywhere at the boundary $\partial\Omega$, while the pressure is imposed with the homogeneous Neumann boundary condition, as shown in Fig. 4.1. We consider the Reynolds number $Re := 1/\nu = 100$ and take a small CFL
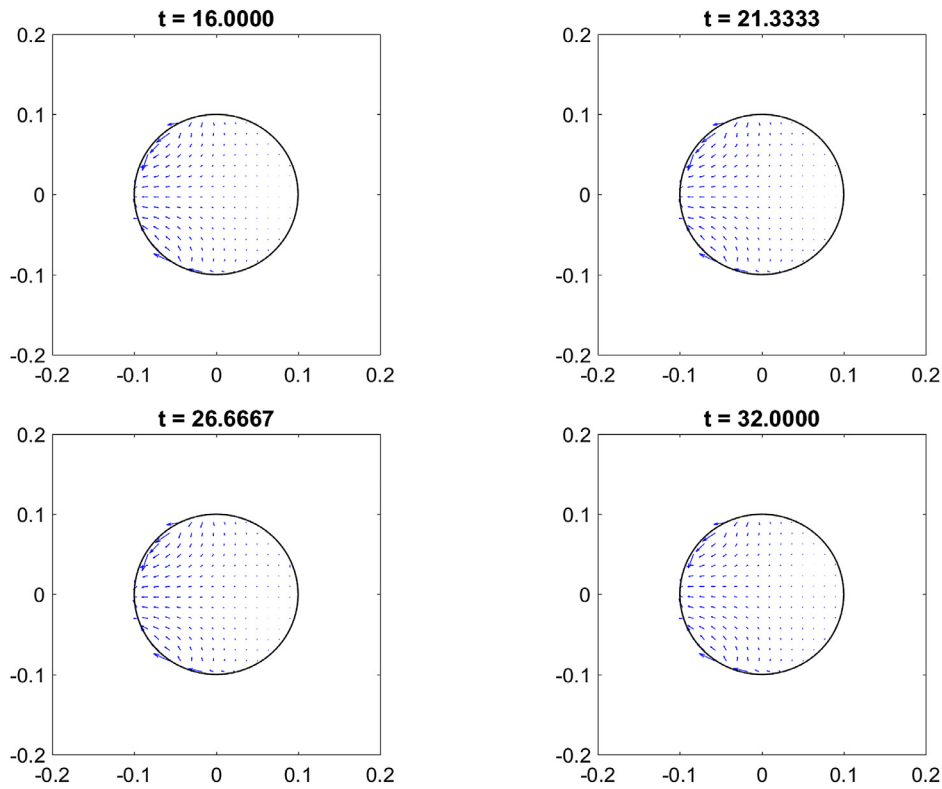
Fig. 4.10. The instantaneous force distribution for $Re = 100$ at different times.
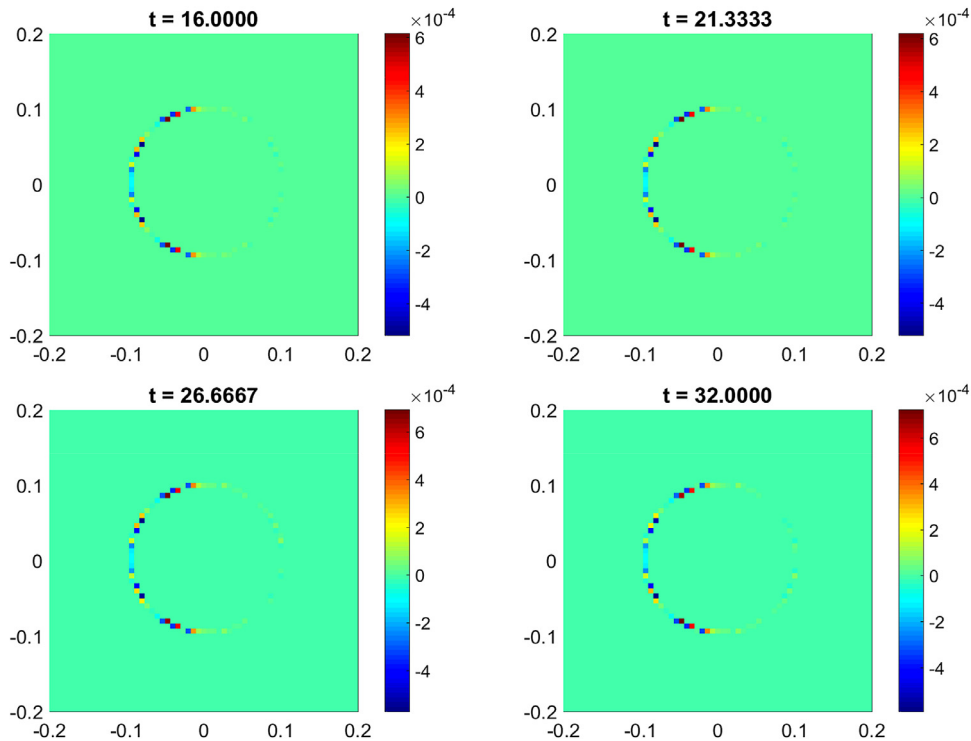
Fig. 4.11. The instantaneous sink-source distribution for $Re = 100$ at different times.

number, $CFL = 0.1$, for mainly focusing on the spatial accuracy test. The initial velocity field at $t = 0$ is set to zero, and will advance to the time $T = 4$, which is sure to reach the steady state. At each time level, only one correction in the PC process will be performed.

Since the exact solution is not available in this example, to compute the error at $T = 4$, we employ the numerical solution

produced by the present method with the finest grid size $h = 1/1620$ as the reference solution. Numerical results for different grid resolutions are reported in Table 4.1, in which we consider the grid sizes $h = 1/20, 1/60, 1/180$ and $1/540$. As we consider the grid size refinement by a factor of $1/3$, the staggered grid points in a coarse grid will still retain in the successive refined grid. Con-
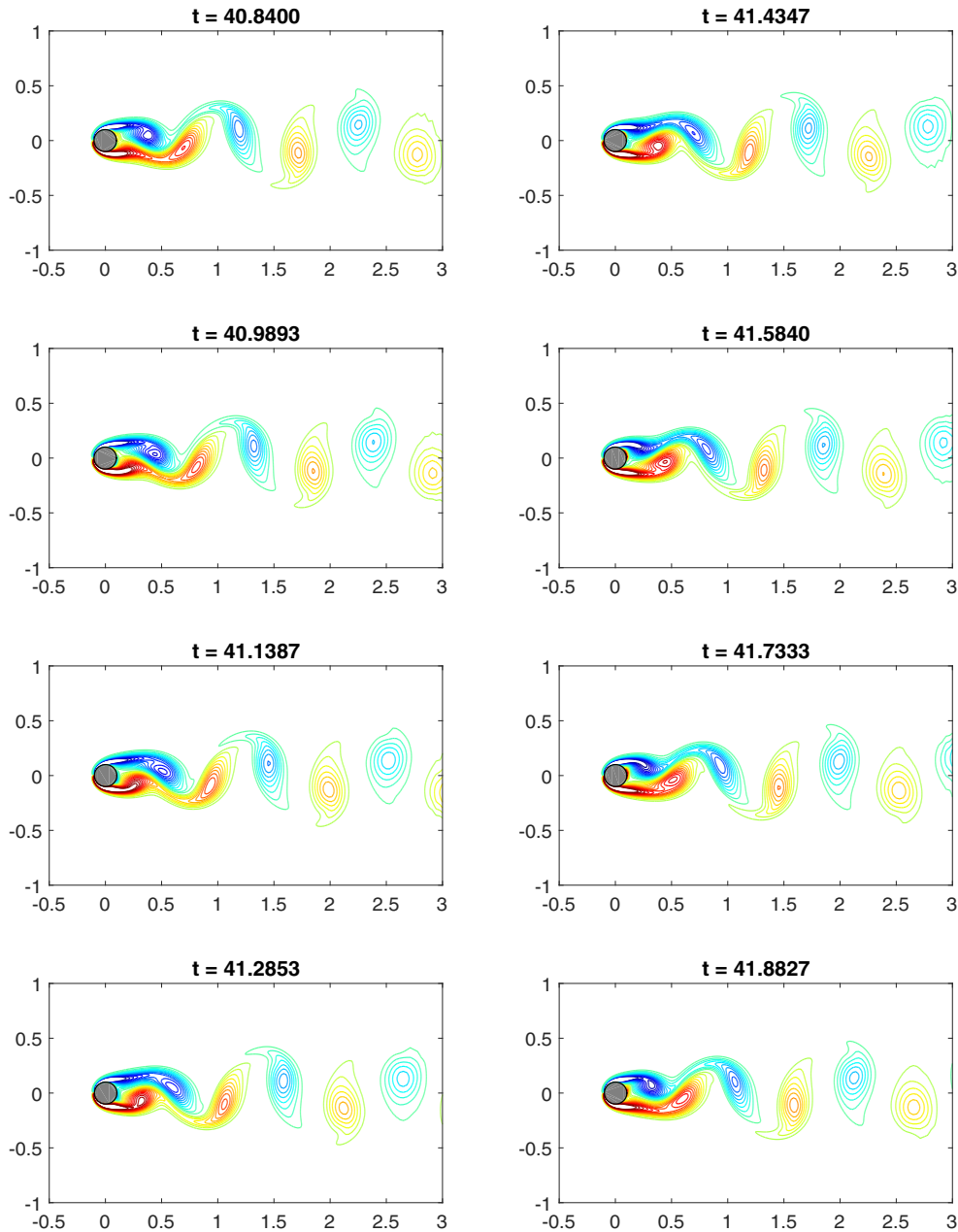
Fig. 4.12. The instantaneous vorticity contours near the oscillating cylinder for $Re = 100$ at different times: (left column) $t \simeq 40.69 + \mathbb{T}/4$, $2\mathbb{T}/4$, $3\mathbb{T}/4$, $\mathbb{T}$; (right column) $t \simeq 40.69 + 5\mathbb{T}/4$, $6\mathbb{T}/4$, $7\mathbb{T}/4$, $2\mathbb{T}$, where $\mathbb{T} \approx 0.595$ is the oscillation period of the cylinder.

sequently, we can estimate the order of convergence of the numerical solutions without any further interpolation processing. In Fig. 4.2, we plot the numerical results of the velocity field and pressure contours at time $t = 4$ produced by the present method with $h = 1/180$.

From the numerical results presented in Table 4.1, we may observe that the order of convergence of the velocity field is apparently better than first order in space in all the 1-norm, 2-norm and maximum norm, while the accuracy of the pressure is of first order accurate in 1-norm and 2-norm and is somewhat nearly half order accurate in the maximum norm. The super-linear convergence, not second-order convergence, in velocity is expected, since we handle the internal velocity boundary condition of the immersed solid body by means of the virtual force $\boldsymbol{F}$ acting on the whole solid domain with the volume-of-solid function η instead of interpolation as in Fadlun et al. [17]. This sacrifice of accuracy in the current vol-
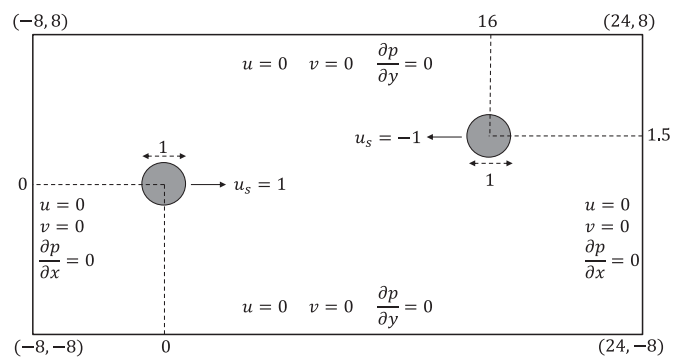
Fig. 4.13. A schematic diagram of the computational domain and boundary conditions for flow around two cylinders moving towards each other.
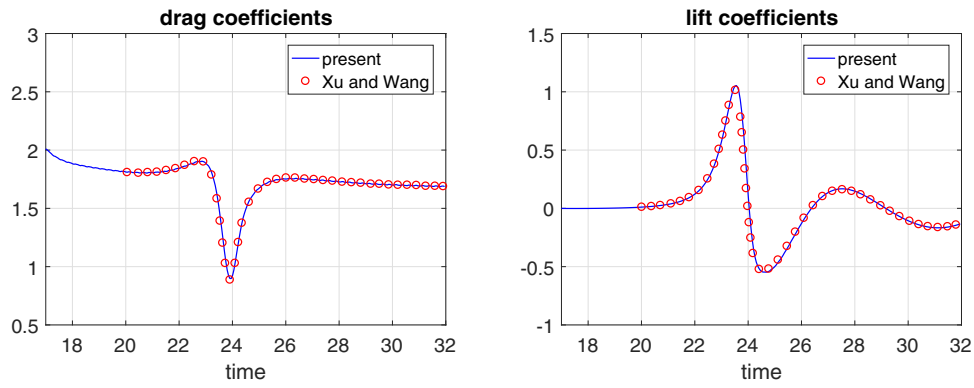
Fig. 4.14. The time evolution of drag and lift coefficients, C_d and C_ℓ, for the upper cylinder in flow around two cylinders compared with the results of Xu and Wang [65].
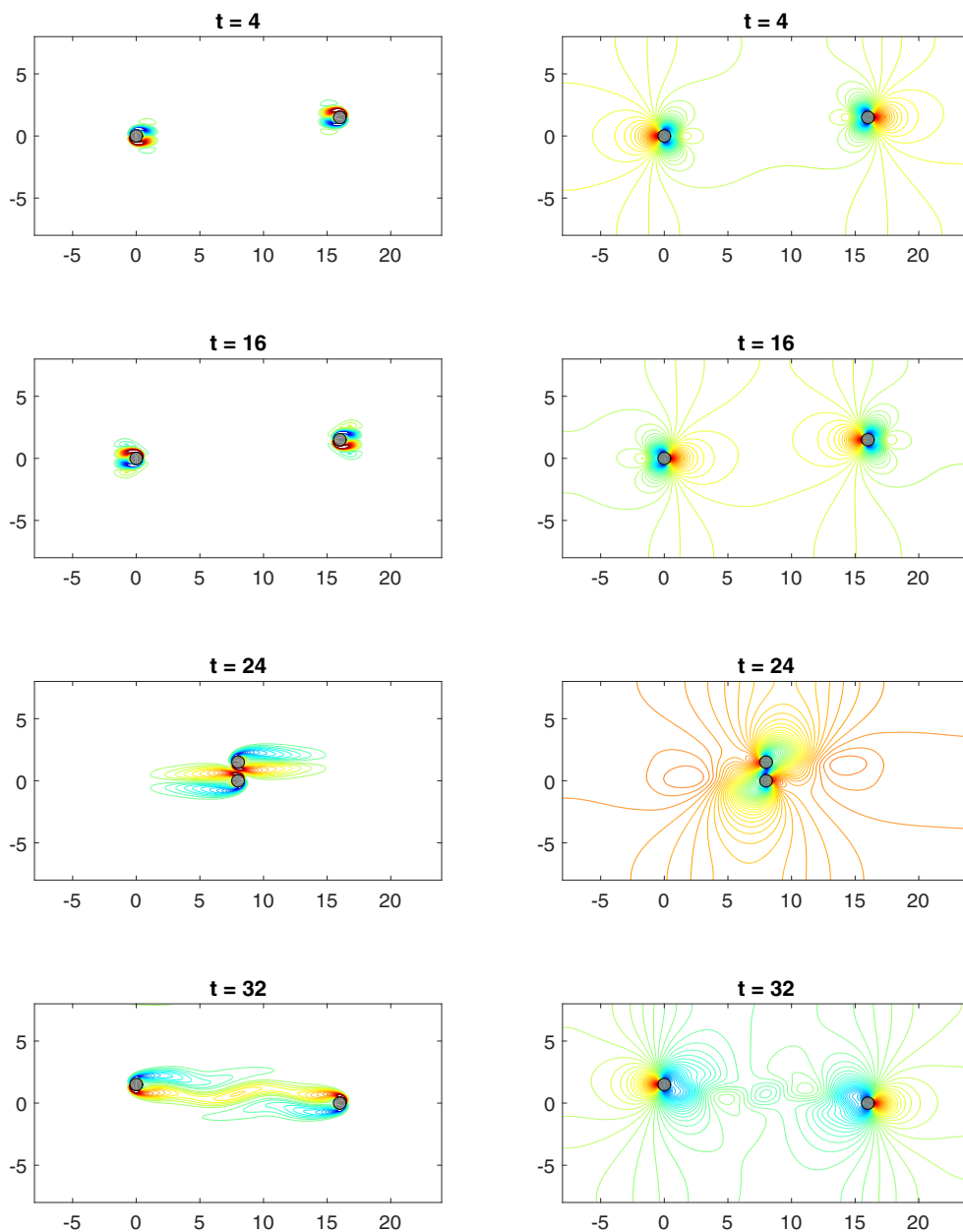
Fig. 4.15. The flow around two cylinders moving towards each other for $Re = 40$ at different times: (left) contours of vorticity; (right) contours of pressure.
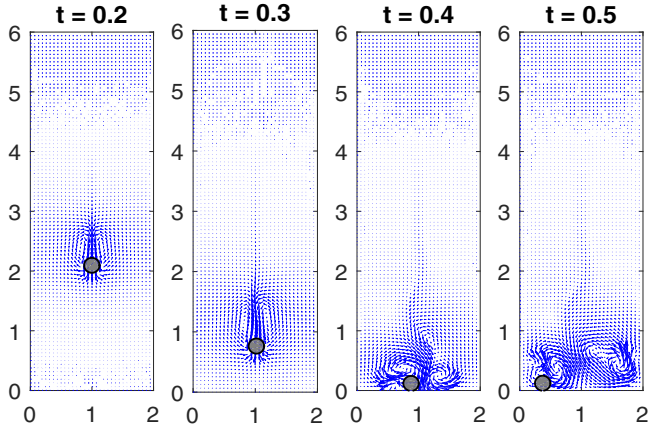
Fig. 4.16. The position of the freely falling solid ball and the flow field visualization at time $t = 0.2, 0.3, 0.4, 0.5$.

ume of solid approach can avoid the additional interpolation procedure at immersed boundary at each time step, and gain the advantage of computing the net force exerted on solid object by fluid easily just by summing up all discrete virtual forces, see e.g., (4.2) below. On the other hand, the lower order of accuracy for pressure than velocity is also expected, since it is inherent in projection scheme. We believe that a more accurate difference scheme in solving the Neumann Poisson problems (3.7)-(3.8) and (3.14)-(3.15) with a careful approximation to the right-hand side data will lead to a better convergence order of the proposed direct-forcing IB projection method with PC. All these issues will be addressed in the future work.

4.2. The flow past a stationary cylinder

The flow past a stationary cylinder, $\boldsymbol{u}_s \equiv \boldsymbol{0}$, is a typical benchmark problem which has been extensively studied both experimentally [14,57] as well as numerically [4,42,54,55,66]. It is well known that the flow configuration depends on the Reynolds number. For low Reynolds number, about $Re \leq 47$, two symmetrical vortices will be stationarily attached behind the cylinder. By increasing the value of Re, the symmetrical vortices will become unstable and break apart, leading to an alternating vortex shedding. In the present study, the settings of simulation parameters are quoted from [54]. We simulate an unsteady flow past a circular cylinder of diameter $D = 0.2$ centered at $(0, 0)$ in the rectangular computational domain $\overline{\Omega} = [-13.4D, 16.5D] \times [-8.35D, 8.35D]$. A constant velocity profile $U_\infty = 1$ is specified at inflow boundary, that is, $x = -13.4D$. The detailed boundary conditions are described in Fig. 4.3. A non-uniform grid of 250×160 cells is adopted to discretize the overall computational domain, within which a uniform grid of 60×60 cells is employed in the subregion $[-D, D] \times [-D, D]$ and the *CFL* number is taken as 0.4. Note that the *CFL* number taken here is rarely large compared with primitive direct-forcing IB methods like Noor et al. [48], in which *CFL* number is usually much smaller since it requires small time step for fluid flow relaxed and adjusted to the immersed solid object. However, through the predicted virtual force $\boldsymbol{F}^{n+\frac{1}{2}, p}$ in the correction stage (3.11), fluid flow is adjusted to the solid object, and therefore it can allow a larger time step.

We introduce three different quantities that are often measured for the sake of comparison with other numerical methods. They are the drag and lift coefficients, and the Strouhal number (cf. [36]). The drag coefficient C_d and the lift coefficient C_ℓ are respec-

tively defined as

$$C_d := \frac{F_d}{U_\infty^2 D/2} \quad \text{and} \quad C_\ell := \frac{F_\ell}{U_\infty^2 D/2}, \tag{4.1}$$

where the drag force F_d and the lift force F_ℓ are respectively approximated by

$$F_d := -\int_\Omega F_1 \, d\boldsymbol{x} \approx -\sum_{\boldsymbol{x}_{ij}} F_1 h^2 \quad \text{and} \quad F_\ell := -\int_\Omega F_2 \, d\boldsymbol{x} \approx -\sum_{\boldsymbol{x}_{ij}} F_2 h^2, \tag{4.2}$$

and $\boldsymbol{F} = (F_1, F_2)$ is the virtual force. All of these quantities are time-varying. When the flow becomes unstable, the stationary vortices behind the cylinder will start moving downstream and shedding alternatively with a frequency f_s. This dimensionless vortex shedding frequency is called the Strouhal number and it is defined as $St := f_s/(U_\infty D)$.

We now consider the simulations at various Reynolds numbers, $Re := U_\infty D/\nu = 20, 40, 100$, to validate the present direct-forcing IB projection method with the PC process. For the cases of $Re = 20$ and $Re = 40$, the computed wake behind the cylinder was seen to be symmetric and steady. The feature of wake is characterized by the non-dimensionalized parameters L_w, a, b and θ as shown in Fig. 4.4, where L_w, a, b, and θ represent the length of the recirculation zone, the distance from the cylinder to the center of the wake vortex, the distance between the centers of the wake vortices, and the separation angle measured from the x-axis, respectively. We compare the numerical results produced by the newly proposed method at time $T = 50$ with those obtained in the literature [4,14,42,54,55,57,66]. The comparison results are listed in Table 4.2, where the experimental studies are indicated with an asterisk *. Moreover, we use the terms "*present method-P*", "*present method-PC*", and "*present method-PCC*" to denote the newly proposed method without correction step (i.e., the method of Noor et al. [48] but with the Choi–Moin projection scheme [9]), with one correction step, and with two correction steps, respectively. We find that our numerical results are in very good agreement with previous works in the literature. In some cases like θ in Table 4.2, present method-PC and present method-PCC show better agreement with literatures than present method-P. We also plot the instantaneous streamline and the corresponding vorticity contours near the cylinder at time $T = 50$ for $Re = 20$ and $Re = 40$ in Fig. 4.6 and 4.5. Here, we remark that while the geometric configurations used in the various methods in Table 4.2 may not be exactly the same, it is widely believed that if the computational domain is large enough than the diameter of the immersed circular cylinder, then we can minimize the effect of the outer boundary on the development of the wake. The computational domain, diameter and center of the circular cylinder of different methods quoted in Table 4.2 (if available) are reported in Table 4.4.

As the Reynolds number increasing, the symmetry of the cylinder wake was broken down and the two vortices shed alternatively. In Table 4.3, numerical results of the maximum drag and lift coefficients at $Re = 100$ for various numerical methods are reported. We can find that for this Reynolds number, the present method without correction generates the drag and lift coefficients that are slightly larger than other numerical results. The time histories of drag and lift coefficients generated by the present method with or without correction step are also depicted in Fig. 4.7, from which we can find that one correction at each time level appears to be good enough for the present direct-forcing IB projection method with PC. Thus, in what follows, we will focus on the present method-PC, unless stated otherwise. Fig. 4.8 and 4.9 shows the time evolution of vorticity and pressure contours of the present method for $Re = 100$. Furthermore, Fig. 4.10 shows the virtual forces distribution and as we have mentioned previ-
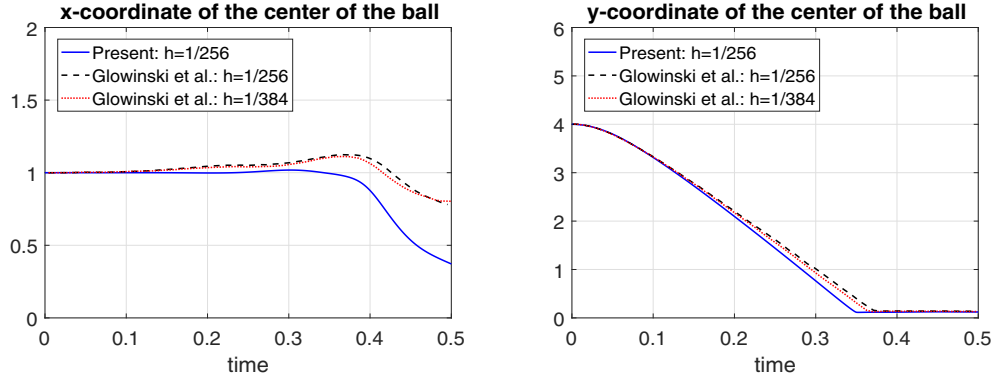
Fig. 4.17. The time evolution of position of the freely falling solid ball in *x*-coordinate (left) and *y*-coordinate (right) compared with the results of Glowinski et al. [18].
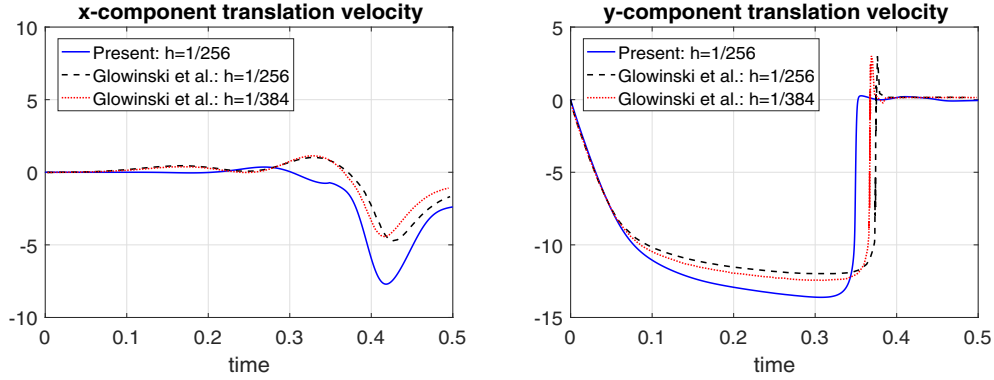
Fig. 4.18. The time evolution of translational velocity of the freely falling solid ball in *x*-component (left) and *y*-component (right) compared with the results of Glowinski et al. [18].

ously, the virtual force acts on the whole solid body. Finally, in Fig. 4.11 we depict the sink-source distribution, which is the distribution of $\int_{\text{cell}} \nabla \cdot \boldsymbol{u}_h \, d\boldsymbol{x}$ for all cells. As we have pointed out at the end of Section 2 that the divergence-free condition may be destroyed in cut cells at which the solid-fluid interface is located, however, in this example we can find that the divergence-free condition of the present method-PC is generally satisfied except only at the leading edge of cylinder. To observe more carefully, these non-zero divergence spots appear as pairs of mass sink and source of equal magnitude (doublet), which upholds global mass conservation. This doublet distribution accompanying particularly large virtual force spots as shown in Fig. 4.10 accommodates jump of pressure gradient at the immersed boundary that has been well analyzed in immersed interface method [35,39,65]. In fact, the idea of doublet is frequently used in source-doublet panel method to compute potential flows [46].

4.3. The flow past an in-line oscillating cylinder

In this subsection, we consider the simulation for the flow past an in-line oscillating cylinder for *Re* = 100 to validate the present method-PC for moving bodies with a prescribed velocity. The computational domain and numerical details are exactly the same as that in Section 4.2, except the cylinder is now oscillating parallel to the free stream at a frequency (f_c) equal to two times the vortex shedding frequency (f_s) of the single fixed cylinder, i.e., $f_c = 2f_s$. The motion of the cylinder is governed by the horizontal velocity as $\boldsymbol{u}_s(t, \boldsymbol{x}) = 0.14D \cos(2\pi f_c t)$, where the amplitude of the oscillation is 0.14 of the cylinder diameter *D*. This simulation has been performed numerically by, e.g., Hurlbut et al. [25], Noor et al. [48], and Su et al. [54].

It has been observed in, e.g., [48], that the in-line oscillation of the cylinder at a range near twice the shedding frequency of the stationary cylinder would cause the resonance and thus largely increase both the drag and lift forces acting on the cylinder. In Table 4.5, we show the comparison of the maximum drag and lift coefficients of the present scheme with the previous studies. One can see that the resonance was successfully captured by the present method. The instantaneous vorticity contours during a period of oscillation are depicted in Fig. 4.12.

4.4. Two cylinders moving towards each other

This example is taken from [51], which provides a demonstration of flow past multiple moving solid objects. In our simulations, we use a uniform grid of 640×320 cells to discretize the computational domain $\overline{\Omega} = [-8, 24] \times [-8, 8]$ and take the time step $\Delta t = 1/200$ for the time-discretization. Thus, the *CFL* number is 0.1. The boundary conditions are specified to be zero velocity and homogeneous Neumann pressure on the whole boundary, see Fig. 4.13. The Reynolds number is set to be 40. The motion of the lower and upper cylinders are governed by setting the dynamics of their centers ($x_{\text{lc}}, y_{\text{lc}}$) and ($x_{\text{uc}}, y_{\text{uc}}$) to

$$x_{\text{lc}} = \begin{cases} \dfrac{4}{\pi} \sin\left(\dfrac{\pi t}{4}\right), & 0 \le t \le 16, \\ t - 16, & 16 \le t \le 32 \end{cases} \quad \text{and} \quad y_{\text{lc}} = 0, \quad (4.3)$$

and

$$x_{\text{uc}} = \begin{cases} 16 - \dfrac{4}{\pi} \sin\left(\dfrac{\pi t}{4}\right), & 0 \le t \le 16, \\ 32 - t, & 16 \le t \le 32 \end{cases} \quad \text{and} \quad y_{\text{uc}} = 1.5. \quad (4.4)$$

Not the that both cylinders will oscillate about their initial positions for two periods, and then toward each other at time *t* = 16.
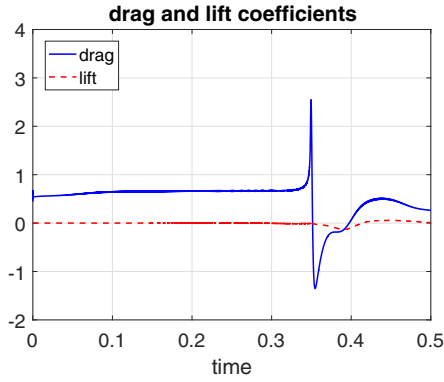
Fig. 4.19. The time evolution of drag and lift coefficients of the freely falling solid ball.

In Fig. 4.14, the time evolution of drag and lift coefficients for the upper cylinder compared with the results of Xu and Wang [65] are displayed. In [65], Xu and Wang implemented an immersed interface method using the same uniform grid but with a very small time step $\Delta t = 1/2000$, which is $1/10$ of the time step used here. The small time step required in [65] is again due to the need for relaxing and adjusting fluid flow to solid objects. However, we can observe that the behaviors of the drag and lift coefficients of both methods are almost the same and they are also consistent very well with the results of [51]. As pointed out in [51], the drag is increasing slightly as the two cylinders approach each other and decreasing to the minimum value when they are closest to each other. After that, the drag then rises back and begins to approximate the profile of a single cylinder. On the other hand, the two cylinders are repulsive when approaching each other and then become attractive after passed each other. Finally, we plot the vorticity and pressure contours at times $t = 4, 16, 24, 32$ in Fig. 4.15, which exhibits the simplicity and high performance of the present two-stage approach.

4.5. A freely falling solid ball

In this section, we simulate the dynamics of a free-falling solid body to validate the ability of the current method for solving two-way coupling problems, where the solid velocity $\boldsymbol{u}_s$ is not prescribed. We consider a 2-D solid ball falling in a rectangular tank filled with an incompressible Newtonian viscous fluid. The settings of simulation are same with that in the work of Glowinski et al. [18]. More specifically, the computational domain is $\overline{\Omega} = [0, 2] \times [0, 6]$, the diameter of the solid ball $\overline{\Omega}_s$ is $D = 0.25$ and the center is located at $(1, 4)$ at the initial time $t = 0$, the density of fluid part is $\rho_f = 1$ and solid part is $\rho_s = 1.5$. In this example, we take the fluid viscosity as $\nu = 0.01$.

To simplify the implementation of current approach, in this example, we apply the two-stage direct-forcing IB method combined with the Chorin first-order in time projection scheme to solve this two-way coupling problem, where we first derive the following initial value problems for the equations of motion of the falling solid ball $\overline{\Omega}_s$:

$$(M_s - M_f)\frac{d\boldsymbol{u}_c}{dt} = (M_s - M_f)\boldsymbol{g} - \int_{\Omega_s} \rho_f \boldsymbol{F} dV, \quad \boldsymbol{u}_c(0) = \boldsymbol{u}_{c0}, \quad (4.5)$$

$$(\boldsymbol{I}_s - \boldsymbol{I}_f)\frac{d\omega}{dt} = -\int_{\Omega_s} \rho_f \boldsymbol{r} \times \boldsymbol{F} dV, \quad \omega(0) = \omega_0, \quad (4.6)$$

where the solid velocity is defined by

$$\boldsymbol{u}_s(t, \boldsymbol{x}) := \boldsymbol{u}_c(t) + \omega(t) \times \boldsymbol{r}(t, \boldsymbol{x}), \quad \boldsymbol{r} := \boldsymbol{x} - \boldsymbol{X}_c, \quad \forall \, \boldsymbol{x} \in \overline{\Omega}_s(t),$$

$$(4.7)$$

with the translational velocity $\boldsymbol{u}_c$, the angular velocity ω, and the centroid $\boldsymbol{X}_c$ of the solid ball $\overline{\Omega}_s$, $M_s := \int_{\Omega_s} \rho_s dV$, $M_f := \int_{\Omega_s} \rho_f dV$, $\boldsymbol{g}$ is the gravity, $\boldsymbol{I}_s$ is the rotational inertia for the solid ball, $\boldsymbol{I}_f$ is the rotational inertia of $\overline{\Omega}_s$ when the portion of the solid ball $\overline{\Omega}_s$ is replaced by the fluid. As we have mentioned in the beginning of Section 2, we treat the solid portion like a fluid, but with an additional virtual force field $\boldsymbol{F} = (F_1, F_2)$ acting on that region. The virtual force $\boldsymbol{F}$ is distributed on the whole region enclosed by the immersed boundary, not only on the immersed boundary, such that the fluid part inside the region would behave like a real solid ball. The governing equations of motion (4.5)-(4.6) of the solid ball is similar to the equations derived in [61], where the virtual force only exists on the immersed boundary. We refer the reader to the Appendix B in [61] for more details.

We then employ the backward Euler scheme to approximate the initial value problems (4.5) and (4.6) to obtain the translational velocity $\boldsymbol{u}_c$, the angular velocity ω, and thus the solid velocity $\boldsymbol{u}_s(t, \boldsymbol{x})$ by (4.7). In our numerical simulation, we take the grid size $h = 1/256$ and a small time step $\Delta t = 7.5e-05$. Below, we present some preliminary numerical results of the free-falling problem to validate the ability of the current method. The position of the freely falling solid ball and the flow field visualization at different time is displayed in Fig. 4.16. The time evolution of position and translational velocity of the solid ball compared with the results of Glowinski et al. [18] are depicted in Fig. 4.17 and Fig. 4.18, respectively. We also show the time evolution of drag and lift coefficients of the freely falling solid ball in Fig. 4.19. In this example, the drag force F_d and the drag coefficient C_d should be calculated by

$$F_d = -\int_\Omega F_2 d\boldsymbol{x} = -\int_{\Omega_s} F_2 d\boldsymbol{x} \approx -\sum_{\boldsymbol{x}_{ij}} F_2 h^2 \quad \text{and} \quad C_d = \frac{F_d}{U_\infty^2 D/2},$$

$$(4.8)$$

and the lift force F_ℓ and lift coefficient C_ℓ should be computed by

$$F_\ell = -\int_\Omega F_1 d\boldsymbol{x} = -\int_{\Omega_s} F_1 d\boldsymbol{x} \approx -\sum_{\boldsymbol{x}_{ij}} F_1 h^2 \quad \text{and} \quad C_\ell = \frac{F_\ell}{U_\infty^2 D/2},$$

$$(4.9)$$

where we use the terminal speed $U_\infty = 12$ of the solid ball relative to the fluid. From these numerical results, we can find that the dynamical behavior is qualitatively similar to that of [18].

To conclude, preliminary numerical simulations indicate that the proposed approach seems to be capable of solving the two-way fluid-solid interaction problems. This study is still in progress and we will report the detailed derivation of the governing equations of motion of the solid ball and the improved numerical algorithms in a future paper.

5. Summary and conclusions

In this paper, we have proposed a simple and novel two-stage direct-forcing IB projection method for simulating the dynamics of fluid-solid interaction problems, where each immersed solid object can be stationary or moving in the fluid with a prescribed velocity. For the consistency consideration, we have adopted the second-order in time Choi–Moin scheme for the projection computations in the proposed method. This approach can be categorized as a direct-forcing method with a PC process, in which a time-discrete virtual force distributed only on the immersed solid bodies is derived, and then added to the fluid momentum equations to accommodate the internal velocity boundary conditions at the immersed

solid boundaries. More specifically, in the prediction stage, based on the rate of moment changes of the solid bodies, we have predicted the virtual force by using the difference between the prescribed solid velocities and the computed velocities, which are obtained by applying the Choi–Moin projection scheme to the incompressible Navier–Stokes equations on the entire domain without adding any virtual forcing term. Then, in the correction stage, we have put the predicted virtual force into the momentum equations as an additional forcing term and performed the Choi–Moin projection again to update the velocity field, pressure and virtual force. Apparently, we can iterate this PC procedure to form a more general $P(C)^k$ method for $k \geq 2$, if necessary.

We have performed numerical experiments of several benchmark problems to illustrate the simplicity and high performance of the newly proposed two-stage method, including the flow induced by a rotating cylinder inside a square enclosure for convergence test, the flow past a stationary cylinder, the flow past an in-line oscillating cylinder, and the flow of two cylinders moving towards each other. In particular, we have found from the convergence test that the order of convergence of the velocity field is apparently better than first order in space in all the 1-norm, 2-norm, and maximum norm, while the accuracy of the pressure is of first order accurate in 1-norm and 2-norm and is somewhat nearly half order accurate in the maximum norm. We have also found that our numerical results are in very good agreement with previous works in the literature and one correction at each time step appears to be good enough for the proposed PC procedure.

We now give the following remarks to conclude this paper:

- We believe that the orders of convergence in space of all unknown functions in the proposed method can be significantly improved by a more accurate difference scheme in solving the Neumann Poisson problems (3.7)-(3.8) and (3.14)-(3.15) with a careful approximation to the right-hand side data.
- Notice that in this paper, the interaction between the fluid part and the solid part is of one-way type, since the motion of the immersed solids is prescribed by a given velocity field $\boldsymbol{u}_s$. However, the underlying ideas of the proposed direct-forcing IB projection method with a PC process could be applied to solve the two-way fluid-solid interaction problems, where the velocity and trajectory of immersed solid object should be governed by the equations of motion depending on fluid flow situation. Indeed, preliminary numerical simulations of the free-falling process of a 2-D solid ball in an incompressible viscous fluid reported in Section 4.5 indicate that the proposed approach seems to be capable of solving the two-way fluid-solid interaction problems.
- The proposed approach in this paper could also be generalized to solve the fluid-elastic body interaction problems, where the elastic structure is modeled by the linear elasticity equations which is assumed to be quasi-static, isotropic and homogeneous and thus undergoes a small deformation.

For these issues, the efforts are in progress and we will report the results in the near future.

Acknowledgments

References

[1] Bell JB, Colella P, Glaz HM. A second-order projection method for the incompressible Navier–Stokes equations. J Comput Phys 1989;85:257–83.

[2] Breugem WP. A second-order accurate immersed boundary method for fully resolved simulations of particle-laden flows. J Comput Phys 2012;231:4469–98.

[3] Brown DL, Cortez R, Minion ML. Accurate projection methods for the incompressible Navier–Stokes equations. J Comput Phys 2001;168:464–99.

[4] Calhoun D. A cartesian grid method for solving the two-dimensional streamfunction-vorticity equations in irregular regions. J Comput Phys 2002;176:231–75.

[5] Chern MJ, Kuan YH, Nugroho G, Lu GT, Horng TL. Direct-forcing immersed boundary modeling of vortex-induced vibration of a circular cylinder. J Wind Eng Ind Aerodyn 2014;134:109–21.

[6] Chern MJ, Noor DZ, Liao CB, Horng TL. Direct-forcing immersed boundary method for mixed heat transfer. Commun Comput Phys 2015;18:1072–94.

[7] Chern MJ, Shiu WC, Horng TL. Immersed boundary modeling for interaction of oscillatory flow with cylinder array under effects of flow direction and cylinder arrangement. J Fluids Struct 2013;43:325–46.

[8] Chiu PH, Lin RK, Sheu TWH. A differentially interpolated direct forcing immersed boundary method for predicting incompressible Navier–Stokes equations in time-varying complex geometries. J Comput Phys 2010;229:4476–500.

[9] Choi H, Moin P. Effects of the computational time step on numerical solutions of turbulent flow. J Comput Phys 1994;113:1–4.

[10] Choi JI, Oberoi RC, Edwards JR, Rosati JA. An immersed boundary method for complex incompressible flows. J Comput Phys 2007;224:757–84.

[11] Chorin AJ. Numerical solution of the Navier–Stokes equations. Math Comput 1968;22:745–62.

[12] Chorin AJ. On the convergence of discrete approximations to Navier–Stokes equations. Math Comput 1969;23:341–53.

[13] Chorin AJ, Marsden JE. A mathematical introduction to fluid mechanics. 2nd. New York: Springer-Verlag; 1990.

[14] Coutanceau M, Bouard R. Experimental determination of the main features of the viscous flow in the wake of a circular cylinder in uniform translation,part 1. steady flow. J Fluid Mech 1977;79:231–56.

[15] Domenichini F. On the consistency of the direct forcing method in the fractional step solution of the Navier–Stokes equations. J Comput Phys 2008;227:6372–84.

[16] E W, Liu JG. Projection method III: spatial discretization on the staggered grid. Math Comput 2001;71:27–47.

[17] Fadlun EA, Verzicco R, Orlandi P, Mohd-Yusof J. Combined immersed-boundary finite-difference methods for three-dimensional complex flow simulations. J Comput Phys 2000;161:35–60.

[18] Glowinski R, Pan TW, Hesla TI, Joseph DD, Périaux J. A fictitious domain approach to the direct numerical simulation of incompressible viscous flow past moving rigid bodies: application to particulate flow. J Comput Phys 2001;169:363–426.

[19] Goldstein D, Handler R, Sirovich L. Modeling a no-slip flow boundary with an external force field. J Comput Phys 1993;105:354–66.

[20] Griffith BE. An accurate and efficient method for the incompressible Navier–Stokes equations using the projection method as a preconditioner. J Comput Phys 2009;228:7565–95.

[21] Guermond JL, Minev P, Shen J. An overview of projection methods for incompressible flows. Comput Methods Appl Mech Eng 2006;195:6011–45.

[22] Guy RD, Hartenstine DA. On the accuracy of direct forcing immersed boundary methods with projection methods. J Comput Phys 2010;229:2479–96.

[23] Harlow FH, Welsh JE. Numerical calculation of time-dependent viscous incompressible flow of fluid with a free surface. Phys Fluids 1965;8:2181–9.

[24] Hsieh PW, Lai MC, Yang SY, You CS. An unconditionally energy stable penalty immersed boundary method for simulating the dynamics of an inextensible interface interacting with a solid particle. J Sci Comput 2015;64:289–316.

[25] Hurlbut SE, Spaulding ML, White FM. Numerical solution for laminar two dimensional flow about a cylinder oscillating in a uniform stream. J Fluids Eng 1982;104:214–20.

[26] Ji C, Munjiza A, Williams JJR. A novel iterative direct-forcing immersed boundary method and its finite volume applications. J Comput Phys 2012;231:1797–821.

[27] Kajishima T, Takiguchi S, Hamasaki H, Miyake Y. Turbulence structure of particle-laden flow in a vertical plane channel due to vortex shedding. JSME Int J Ser B, 2001;44:526–35.

[28] Kajishima T, Takiguchi S. Interaction between particle clusters and particle-induced turbulence. Int J Heat Fluid Flow, 2002;23:639–46.

[29] Kempe T, Fröhlich J. An improved immersed boundary method with direct forcing for the simulation of particle Laden flows. J Comput Phys 2012;231:3663–84.

[30] Kim J, Kim D, Choi H. An immersed-boundary finite-volume method for simulations of flow in complex geometries. J Comput Phys 2001;171:132–50.

[31] Kim J, Moin P. Application of a fractional-step method to incompressible Navier–Stokes equations. J Comput Phys 1985;59:308–23.

[32] Kim Y, Lai MC. Simulating the dynamics of inextensible vesicles by the penalty immersed boundary method. J Comput Phys 2010;229:4840–53.

[33] Kim Y, Peskin CS. Penalty immersed boundary method for an elastic boundary with mass. Phys Fluids 2007;19:053103.

[34] Lai MC, Hu WF, Lin WW. A fractional step immersed boundary method for stokes flow with an inextensible interface enclosing a solid particle. SIAM J Sci Comput 2012;34:B692–710.

[35] Lai MC, Li Z. A remark on jump conditions for the three-dimensional Navier-Stokes equations involving an immersed moving membrane. Appl Math Lett 2001;14:149–54.

[36] Lai MC, Peskin CS. An immersed boundary method with formal second-order accuracy and reduced numerical viscosity. J Comput Phys 2000;160:705–19.

[37] Lai MC, Tseng YH, Huang H. An immersed boundary method for interfacial flow with insoluble surfactant. J Comput Phys 2008;227:7279–93.

[38] Le DV, Khoo BC, Lim KM. An implicit-forcing immersed boundary method for simulating viscous flows in irregular domains. Comput Methods Appl Mech Eng 2008;197:2119–30.

[39] Li Z, Lai MC. The immersed interface method for the Navier-Stokes equations with singular forces. J Comput Phys 2001;171:822–42.

[40] Liao CC, Chang YW, Lin CA, McDonough JM. Simulating flows with moving rigid boundary using immersed-boundary method. Comput Fluids 2010;39:152–67.

[41] Silva ALFLE, Silveira-Neto A, Damasceno JJR. Numerical simulation of two-dimensional flows over a circular cylinder using the immersed boundary method. J Comput Phys 2003;189:351–70.

[42] Linnick MN, Fasel HF. A high-order immersed interface method for simulating unsteady incompressible flows on irregular domains. J Comput Phys 2005;204:157–92.

[43] Liu C, Zheng X, Sung CH. Preconditioned multigrid methods for unsteady incompressible flows. J Comput Phys 1998;139:35–57.

[44] Luo H, Dai H, de Sousa PJSAF, Yin B. On the numerical oscillation of the direct-forcing immersed-boundary method for moving boundaries. Comput Fluids 2012;56:61–76.

[45] Mittal R, Iaccarino G. Immersed boundary methods. Ann Rev Fluid Mech 2005;37:239–61.

[46] Morino L, Chen LT, Suciu EO. Steady and oscillatory subsonic and supersonic aerodynamics around complex configurations. AIAA J 1975;13:368–74.

[47] Newren EP, Fogelson AL, Guy RD, Kirby RM. Unconditionally stable discretizations of the immersed boundary equations. J Comput Phys 2007;222:702–19.

[48] Noor DZ, Chern MJ, Horng TL. An immersed boundary method to solve fluid–solid interaction problems. Comput Mech 2009;44:447–53.

[49] Peskin CS. Flow patterns around heart valves: a numerical method. J Comput Phys 1972;10:252–71.

[50] Peskin CS. The immersed boundary method. Acta Numer 2002;11:479–517.

[51] Russell D, Wang ZJ. A cartesian grid method for modeling multiple moving objects in 2d incompressible viscous flow. J Comput Phys 2003;191:177–205.

[52] Saiki EM, Biringen S. Numerical simulation of a cylinder in uniform flow: application of a virtual boundary method. J Comput Phys 1996;123:450–65.

[53] Stockie JM, Wetton BR. Analysis of stiffness in the immersed boundary method and implications for time-stepping schemes. J Comput Phys 1999;154:41–64.

[54] Su SW, Lai MC, Lin CA. An immersed boundary technique for simulating complex flows with rigid boundary. Comput Fluids 2007;36:313–24.

[55] Taira K, Colonius T. The immersed boundary method: a projection approach. J Comput Phys 2007;225:2118–37.

[56] Temam R. Sur l'approximation de la solution des équations de Navier-Stokes par la méthode des pas fractionnaires II. Arch Rat Mech Anal 1969;33:377–385.

[57] Temam R. Navier-Stokes equations: theory and numerical analysis, revised edition, Elsevier Science PublishersB.V., Amsterdam. 1984.

[58] Tritton DJ. Experiments on the flow past a circular cylinder at low Reynold's numbers. J Fluid Mech 1959;6:547–67.

[59] Tseng YH, Ferziger JH. A ghost-cell immersed boundary method for flow in complex geometry. J Comput Phys 2003;192:593–623.

[60] Tu C, Peskin CS. Stability and instability in the computation of flows with moving immersed boundaries: a comparison of three methods. SIAM J Sci Stat Comput 1992;13:1361–76.

[61] Uhlmann M. An immersed boundary method with direct forcing for the simulation of particulate flows. J Comput Phys 2005;209:448–76.

[62] Vanella M, Rabenold P, Balaras E. A direct-forcing embedded-boundary method with adaptive mesh refinement for fluid-structure interaction problems. J Comput Phys 2010;229:6427–49.

[63] van der Vorst HA. Bi-CGSTAB: a fast and smoothly converging variant of bi-CG for the solution of nonsymmetric linear systems. SIAM J Sci Stat Comput 1992;13:631–44.

[64] Wang Z, Fan J, Luo K. Combined multi-direct forcing and immersed boundary method for simulating flows with moving particles. Int J Multiph Flow 2008;34:283–302.

[65] Xu S, Wang ZJ. An immersed interface method for simulating the interaction of a fluid with moving boundaries. J Comput Phys 2006;216:454–93.

[66] Ye T, Mittal R, Udaykumar HS, Shyy W. An accurate cartesian grid method for viscous incompressible flows with complex immersed boundaries. J Comput Phys 1999;156:209–40.

[67] You CS. On two immersed boundary methods for simulating the dynamics of fluid-structure interaction problems, Ph.D. Dissertation. Taiwan,: Department of Mathematics, National Central University; 2016.

[68] Zhang N, Zheng ZC. An improved direct-forcing immersed-boundary method for finite difference applications. J Comput Phys 2007;221:250–68.

[69] Zheng Z, Petzold L. Runge-Kutta-Chebyshev projection method. J Comput Phys 2006;219:976–91.